HAL open science

Viscoplasticity and growth strain parameters identification by full modelling optimization during the high temperature oxidation of Ni28Cr modified by the reactive element yttria or zirconium

Zhimao Wang, Jean-Luc Grosseau-Poussard, Benoît Panicaud, Guillaume Geandier, Pierre-Olivier Renault, Philippe Goudeau, Nathalie Boudet, Nils Blanc, Felaniaina Rakotovao, Zhaojun Tao

To cite this version:

Zhimao Wang, Jean-Luc Grosseau-Poussard, Benoît Panicaud, Guillaume Geandier, Pierre-Olivier Renault, et al.. Viscoplasticity and growth strain parameters identification by full modelling optimization during the high temperature oxidation of Ni28Cr modified by the reactive element yttria or zirconium. Computational Materials Science, 2020, 180, pp.109689. 10.1016/j.commatsci.2020.109689 . hal-02547434

HAL Id: hal-02547434

https://utt.hal.science/hal-02547434v1

Submitted on 22 Aug 2022

HAL is a multi-disciplinary open access archive for the deposit and dissemination of scientific research documents, whether they are published or not. The documents may come from teaching and research institutions in France or abroad, or from public or private research centers.

L'archive ouverte pluridisciplinaire **HAL**, est destinée au dépôt et à la diffusion de documents scientifiques de niveau recherche, publiés ou non, émanant des établissements d'enseignement et de recherche français ou étrangers, des laboratoires publics ou privés.

Distributed under a Creative Commons Attribution - NonCommercial 4.0 International License

Version of Record: https://www.sciencedirect.com/science/article/pii/S0927025620301804
Manuscript_a5161cf53353963326355ceb2efcfaf9

Viscoplasticity and growth strain parameters identification by full modelling optimization during the high temperature oxidation of Ni28Cr modified by the reactive element yttria or zirconium

Zhimao Wang [1], Jean-Luc Grosseau-Poussard [2], Benoît Panicaud [1*], Guillaume Geandier [3], Pierre-Olivier Renault [4], Philippe Goudeau [4], Nathalie Boudet [5,6], Nils Blanc [5,6], Felaniaina Rakotovao [2], and Zhaojun Tao [1]

[1] Université de Technologie de Troyes (UTT), Institut Charles Delaunay (ICD), Systèmes Mécaniques et d'Ingénierie Simultanée (LASMIS), 12 rue Marie Curie, CS 42060, 10004, Troyes Cedex, France;

[2] Laboratoire des Sciences de l'Ingénieur pour l'Environnement (LaSIE), Université de La Rochelle, CNRS UMR 7356, Avenue Michel Crépeau, 17042, La Rochelle Cedex 1, France;

[3] Institut Jean Lamour, CNRS UMR 7198, Université de Lorraine, Campus ARTEM, 2 Allée Andrée Guinier, BP 50840, 54011 Nancy Cedex, France

[4] Institut P', CNRS UPR 3346, Université de Poitiers, SP2MI - 11 Boulevard Marie et Pierre Curie, BP 30179, 86962 Futuroscope, France

[5] CNRS, Institut Néel, 38042 Grenoble Cedex, France

[6] Université Grenoble Alpes, Institut Néel, 38042, Grenoble Cedex, France

* Correspondence: benoit.panicaud@utt.fr; Tel.: +333 25 71 80 61

Received: date; Accepted: date; Published: date

Abstract: Chromium-based alloys have been developed to form chromia layers in oxidizing environments for high temperature applications, providing a good protection against further oxidation. The mechanical behavior and oxide layer growth of yttria-coated or zirconium-doped Ni28Cr alloy are presently studied under high temperature oxidation conditions. These kind of reactive elements can decrease oxidation kinetics and significantly increase the adhesion of chromia layer on the metallic substrate. However, during oxidation, a compressive stress generally occurs in thermally grown oxide (TGO) due to the oxide layer and its mechanical interaction with the metallic substrate. These growth stresses, combined with the thermal stresses that develop during temperature changes, may initiate and cause layer cracking or spallation, which limits the lifetime of alloys in such a challenging environment. For prediction of this lifetime, it is important to know with accuracy the thermomechanical behavior of such a system. Therefore, a thermomechanical modelling is proposed and applied to optimize numerically the unknown parameters, especially viscoplastic ones. For the raw material and modified materials by reactive elements, the creep parameter decreases with a lower temperature, which means that the viscoplastic strain decreases with a decreasing temperature. For the yttria-coated or zirconium-doped material, the main result is an increase of the activation energy of this creep parameter with the quantity of reactive element.

Keywords: Thermomechanical modelling ; In-situ X-ray diffraction ; Thermally grown oxide ; Chromia forming alloy ; Reactive elements ; Viscoplasticity parameter ; Growth strain parameter ; Activation energy

© 2020 published by Elsevier. This manuscript is made available under the CC BY NC user license
https://creativecommons.org/licenses/by-nc/4.0/

1. Introduction

1.1. Background and Motivations

During the oxidation of a metal or metallic alloy at high temperature, an oxide layer is usually formed. Chromium-based alloys have been developed to form chromia layer in oxidizing atmospheres for high temperature applications, such as nuclear power plant, thermal power station, gas turbine etc. This chromia layer generally provides a good chemical protection against further oxidation. During this oxidation and due to the interface adhesion between the oxide layer and the metallic substrate, a compressive stress generally arises in the thermally grown oxide (TGO) layer. The stresses produced by the oxide development can affect the mechanical balance of the structure and the properties of the metal [1-3].

Concerning this stress generation, there are two main sources of stresses in the oxide layer. One of these sources is the growth stress due to the oxide growth, even during isothermal oxidation. The second one is the thermal stress due to the temperature change with time, and due to the mismatch of the thermal expansion coefficients between the oxide layer and the metallic substrate.

Concerning stress relaxation, an oxide creep is generally concerned rather than delamination, for chromia stressed at sufficiently high temperatures and fine-grained oxide according to Ashby map. Indeed, creep releases the growth stresses in the fine-grained chromia layer, whose grain usually ranges from 0.2 to 0.8 μm [4–6]. In previous works, in-situ strain relaxation studies in the chromia layers were carried out after imposing a sudden temperature change, which introduced an additional stress due to the mismatch between the thermal expansion coefficients of the oxide and the alloy. Relaxation rates were then found to be proportional to stress power σ^n, with $n \leq 2$, which is consistent with a diffusion-creep mechanism [4]. The corresponding creep parameters were first determined in thermally growing chromia layers [5]. In addition, thermal creep activation was studied. The associated elementary mechanism responsible for chromia creep behavior was identified as the inward transport of oxygen [7].

To improve the protective properties of the thermally grown chromia layer under high temperature oxidation, reactive elements are often introduced into the bulk or on the surface of a metallic alloy. In the present study, we mainly use separately two kinds of reactive elements: yttrium oxide (Y_2O_3 / yttria) and zirconium (Zr). Such kind of reactive elements have been shown to decrease the oxidation kinetics and significantly increase the adhesion of chromia layer to the metallic substrate [8-10]. Few researches have been done to demonstrate the possible influence of different quantities of such reactive elements on creep behavior of the oxide layer.

1.2. Aims of the Work

The present work aims to better understand the underlying physical mechanisms and the quantitative influence of different quantities of reactive elements, especially on the creep behavior in oxide layer. We study the time–dependent stresses evolution, which are obtained by treating the results of in-situ high temperature synchrotron diffraction measurements obtained at European Synchrotron Radiation Facility. The $\sin^2\psi$ analysis method provides these time–dependent stresses in the oxide layer.
One aim is to propose an adapted thermomechanical model for the {metal+oxide} system evolution, which allows us to identify the main physical parameters from the experiments. With such a thermomechanical model, we should better understand the underlying physical mechanisms, and especially those responsible for the creep behavior. In addition, with the presence of different reactive elements, the surface properties and creep behavior is also modified, which can help us to understand how it may increase the lifetime of the metallic alloys.

To achieve such a goal and to identify the parameters, which are unknown or unsure, it is also required to investigate a numerical solution of this thermomechanical modelling. Therefore, an adapted method is applied to process the experimental results. By comparing the time–dependent stresses and the numerical solution, thermomechanical and physicochemical parameters can be numerically optimized such as creep parameter and/or growth strain parameter. Such parameters can then be investigated to determine the activation energy associated to the corresponding mechanisms.

2. Thermomechanical modelling for {metal+oxide} systems

2.1 Compositions of strain

To obtain an accurate thermomechanical modelling, some hypotheses are considered:

- For all the materials, the system is isotropic and homogeneous; in other words, it has the same properties in all directions and for all positions.
- For all the materials, the system is under in-plane stress condition.
- For all the materials, the system has neither elastic limit nor hardening behavior; its behavior is directly elasto-viscoplastic.

2.1.1 Elastic part

The classical Hooke model is used for the elastic strain $\varepsilon^{elastic}$ in the metal and in the oxide [11], for an in-plane stress:

$$\varepsilon^{elastic} = \left(\frac{1-\nu}{E}\right)\sigma \tag{1}$$

In a rate formalism [4], by use of the time derivative of Eq. (1), it leads to:

$$\frac{d\varepsilon^{elastic}}{dt} = \frac{d}{dT}\left(\frac{1-\nu}{E}\right)\frac{dT}{dt}\sigma + \left(\frac{1-\nu}{E}\right)\frac{d\sigma}{dt} \tag{2}$$

To obtain this equation, Poisson's ratio ν is supposed to be temperature independent and Young's modulus E is supposed to be temperature dependent, according to a polynomial function [1]:

$$E(T) = a_0 - a_1 T - a_2 T^2 \tag{3}$$

where a_i are constant and temperature independent.

2.1.2 Viscoplastic part

A Norton-Hoff power law is used to simulate the viscoplastic strain $\varepsilon^{viscoplastic}$, as usually considered in the metal and in the oxide [11], for an in-plane stress:

$$\frac{d\varepsilon^{viscoplastic}}{dt} = \mathrm{sign}(\sigma) J |\sigma|^N = \frac{1}{2}\mathrm{sign}(\sigma)\left(\frac{|\sigma|}{K}\right)^N \text{ and } N \in R \tag{4}$$

where J and K are the creep parameters ($J = \frac{1}{2}\left(\frac{1}{K}\right)^N$) and N is the Norton exponent. It is already a rate form. We assume that stress release is caused mostly by creep diffusion in the oxide layer, which is regulated by the transport of chemical species along grain boundaries. The same approach as described in Refs. [12-14] has been applied, with a stress exponent value equal to unity in the Norton flow model. The Norton coefficient J for the oxide is given by:

$$J_{ox} = \frac{AD_0\delta\Omega}{k_B T}\left(\frac{1}{L}\right)^3 \exp\left(-\frac{Q}{RT}\right) \tag{5}$$

where A is Coble constant without dimension, D_0 is diffusion coefficient, δ is the grain boundary average thickness, Ω is the molar volume, k_B is Boltzmann constant, L is the grain size and Q is the activation energy of the mechanism.

2.1.3 Thermomechanical part

For thermal strain $\varepsilon^{thermal}$ in the metal and in the oxide, classical thermal expansion is considered [11]:

$$\frac{d\varepsilon^{thermal}}{dt} = \alpha(T)\frac{dT}{dt} \tag{6}$$

A rate formalism has been applied to obtain Eq. (6). The thermal expansion coefficient α may vary with temperature T [11] with a polynomial function:

$$\alpha(T) = b_0 - b_1 T - b_2 T^2 \tag{7}$$

where b_i are constants and temperature independent.

2.1.4 Growth strain part only for oxide

In the present modelling, the Clarke approaches is used, which was originally proposed in [15] and has been verified and generalized by Panicaud et al. [16]. The growth strain rate is proportional to the oxide layer kinetics:

$$\frac{d\varepsilon^{growth}}{dt} = D_{ox}(T)\frac{dh_{ox}}{dt} \tag{8}$$

For the growth strain parameter D_{ox}, it is more difficult to explicit the expression because the mechanisms depends on the considered system. For the present one, it is not yet fully established. We know that the $D_{ox}(T)$ parameter depends on microstructural features and may also depend on temperature [5]. The temperature dependence $D_{ox}(T)$ adapted to the present material may be:

$$D_{ox}^{-1} = D_{ox0}^{-1}\exp\left(-\frac{Q_D}{RT}\right) \tag{9}$$

where D_{ox0} is an initial parameter for the present oxide, as proposed in [5]. Q_D corresponds to an activation energy for the growth strain parameter. The D_{ox} parameter may be also related to the ratio of the cationic/anionic flux occurring within the grain boundaries as the oxide layer grows [15]. Since both flows follow an Arrhenius dependence, the current activation energy in Eq. 9 may be interpreted as the difference between the values associated with the anionic and cationic flows.

The oxide thickness h_{ox} follows a parabolic evolution with oxidation time t that has already been experimentally evidenced for the present material with experimental characterization by Thermal Gravimetric Analysis [5, 6]. h_{ox} is the thickness of the oxide layer evolving with time:

$$h_{ox} = Ap\sqrt{t} \tag{10}$$

$$\frac{dh_{ox}}{dt} = \frac{Ap}{2\sqrt{t}} + \frac{dAp}{dT}\frac{dT}{dt}\sqrt{t} \tag{11}$$

with Ap the parabolic kinetics parameter that varies with temperature T. In the range of studied temperature, Ap is in the range 2.3 10^{-9} to 1.8 10^{-7} m.s$^{-0.5}$ [5, 6].

2.2 Thermomechanical modelling

2.2.1 Continuity condition for interface displacement

To systematically ensure the continuity condition during all the oxidation time of the metal, the following assumptions have to be assumed:

- The two-dimensional effects such as rumpling are not considered.
- The non-linear mechanical phenomena (buckling, cracking, spalling) are not considered.

Moreover, temperature may evolve with time, but no space gradient of temperature is considered.

Because of the adherence between oxide layer and metallic substrate, after calculations, the continuity equation can be expressed as, for all time:

$$\varepsilon_m = \varepsilon_{ox} \tag{12}$$

With the proposed strain decomposition, it leads to:

$$\left(\varepsilon^{elastic} + \varepsilon^{viscoplastic} + \varepsilon^{thermal}\right)_m = \left(\varepsilon^{elastic} + \varepsilon^{viscoplastic} + \varepsilon^{thermal} + \varepsilon^{growth}\right)_{ox} \tag{13}$$

In a rate formalism, it corresponds to:

$$\left(\frac{d\varepsilon^{elastic}}{dt} + \frac{d\varepsilon^{viscoplastic}}{dt} + \frac{d\varepsilon^{thermal}}{dt}\right)_m = \left(\frac{d\varepsilon^{elastic}}{dt} + \frac{d\varepsilon^{viscoplastic}}{dt} + \frac{d\varepsilon^{thermal}}{dt} + \frac{d\varepsilon^{growth}}{dt}\right)_{ox} \tag{14}$$

2.2.2 Mechanical balance

To calculate the stresses evolution during the oxidation of a metal, the following assumptions are made:

- The system has an isotropic and biaxial behavior (stress state).
- Chemical strain due to the dissolution of oxygen within the substrate alloy is not considered.
- Symmetrical oxidation of the two metallic sides is considered.

Fig. 1 presents the geometry for the oxide growth on a metal. Thus, the equation of mechanical balance can be expressed as:

$$\int_0^{h_m} \sigma_m(z)dz + 2\int_0^{h_{ox}} \sigma_{ox}\, dz = 0 \tag{15}$$

Where σ_{ox} is the stress in the oxide, h_{ox} is the oxide thickness that depends on time t, $\sigma_m(z)$ is the stress in the substrate that depends on z, and h_m is the thickness of the substrate [17]. The influence of the oxide on the top and bottom surfaces is the main effect, which causes the apparition of residual stresses parallel to the oxide-metal interface in the metal. A symmetric oxidation is considered, thanks to the coefficient 2 in the mechanical balance in Eq. (15).

By considering a homogeneous stress (σ_m) distribution in metal and oxide, the mechanical balance equation overall metal and oxide can be expressed as:

$$\sigma_m h_m + 2\sigma_{ox} h_{ox} = 0 \tag{16}$$

In rate form, it corresponds to:

$$\dot{\sigma}_m h_m + 2\dot{\sigma}_{ox} h_{ox} + 2\sigma_{ox}\dot{h}_{ox} = 0 \tag{17}$$

Moreover, because of h_m and h_{ox} are positive number, we have:

$$\mathrm{signe}(\sigma_m) = -\mathrm{signe}(\sigma_{ox}) \tag{18}$$

2.3 Evolution equation for oxide stress and input parameters

For further application, we propose to solve this problem under isothermal condition. Eq. (1)–(18) are simplified to obtain the equation describing the oxide stress evolution with time. It leads to an ordinary differential equation:

$$\dot{\sigma}_{ox} = \frac{\frac{\sigma_{ox}}{t}\frac{1-\nu_m}{E_m} - \mathrm{signe}(\sigma_{ox})\left(\frac{h_m}{Ap\sqrt{t}}\right)^{1-N_m} J_m|\sigma_{ox}|^{N_m} + \mathrm{signe}(\sigma_{ox})J_{ox}|\sigma_{ox}|^{N_{ox}}\frac{h_m}{Ap\sqrt{t}} + \frac{D_{ox}h_m}{2t}}{\left(\frac{1-\nu_{ox}}{E_{ox}}\frac{h_m}{Ap\sqrt{t}} + 2\frac{1-\nu_m}{E_m}\right)} \tag{19}$$

There are 1 geometrical parameter and **10** material parameters to be identified: h_m, ν_m, E_m, ν_{ox}, E_{ox}, Ap, J_m, N_m, J_{ox}, N_{ox} and D_{ox}.

h_m is the thickness of metal part, which can be easily measured and are supposed to be constant. Numerical values of Young's modulus of oxide Cr_2O_3 (E_{ox}) and Poisson's ratio of oxide Cr_2O_3 (ν_{ox}) can be found in literature [20]. Numerical values of the others parameters can also be found in literature [21] for raw material and for different temperatures, such as the Young's modulus of metal (E_m), Poisson's ratio of metal (ν_m), the parabolic kinetics parameter (Ap), the creep parameter of oxide Cr_2O_3 (J_{ox}), the Norton exponent of oxide Cr_2O_3 (N_{ox}), the creep parameter of metal (J_m), the Norton exponent of metal (N_m) and the growth strain parameter for oxide Cr_2O_3 (D_{ox}).

However, to our knowledge, no research was ever undertaken to analyze the evolution of these parameters under the influence of different quantities and nature of different reactive elements. We assume that these reactive elements introduced either by Physical Vapor Deposition (PVD) or by ionic implantation cannot influence significantly the elastic properties of oxide and metal (ν_m, E_m, ν_{ox} and E_{ox}). For the Norton exponent (N_m,N_{ox}), it is assumed at first approximation that they will not evolve significantly with the reactive elements. The same is considered for J_m by considering that the bulk properties of the metal are not affected. This argument can be also considered for neglecting the elastic properties modifications in the metal. At the contrary, these reactive elements are well known

to decrease the oxidation kinetics of the alloy and significantly increase the adhesion of the chromia layer to the metallic substrate [8-10]; it can also modified the growth mechanisms of the oxide layer. Therefore, we focus our investigations on the influence of these reactive elements on the creep parameter of oxide Cr_2O_3 (J_{ox}) and the growth strain parameter for oxide Cr_2O_3 (D_{ox}). At first approximation, the influence on Ap will be neglected and treated in a further publication.

2.4 Numerical method for resolution

The Cauchy problem given by Eq. (19) can be solved as:

$$\dot{\sigma}_{ox} = f(\sigma_{ox}(t), t),\ \sigma_{ox}(t_0) = \sigma_0 \tag{20}$$

where σ_{ox} is an unknown function of time t; $\dot{\sigma}_{ox}$ is the derivative function of the stress depending on t and σ_{ox} itself; at the initial time t_0, σ_{ox} has the value σ_0 and the function f, t_0 and σ_0 are known. To solve this kind of problem, a classical Runge-Kutta resolution scheme is applied [22, 23].

$$\begin{cases} \sigma_{ox,n+1} = \sigma_{ox,n} + \frac{\Delta t}{6}(k_1 + 2k_2 + 2k_3 + k_4) \\ k_1 = f(t_n, \sigma_{ox,n}) \\ k_2 = f\left(t_n + \frac{\Delta t}{2}, \sigma_{ox,n} + \frac{\Delta t}{2}k_1\right) \\ k_3 = f\left(t_n + \frac{\Delta t}{2}, \sigma_{ox,n} + \frac{\Delta t}{2}k_2\right) \\ k_4 = f(t_n + \Delta t, \sigma_{ox,n} + \Delta t k_3) \\ t_{n+1} = t_n + \Delta t, n = 0,1,2,3 \ldots \end{cases} \tag{21}$$

The influence of the time step has been tested. Fig. 2 shows that by changing the time step Δt, the evolution of simulation is quite similar. It is known that a smaller time step leads to a more accurate numerical calculation, which is obviously a disadvantage to the total calculation time. The results indicate that the difference is only significant for the inflection zone. Moreover, the precision increases with the reduction of the time step, its choice has a very small influence, which enables a good compromise with the total calculation time. Therefore, we will now assume that the influence of the time step is negligible if it is chosen relatively small. We have chosen a time step of 0.5 seconds for the calculation for a total oxidation time of several hours. By using the previous Runge-Kutta method, the numerical solution of Eq.19 can be obtained.

3. Materials and Data treatment

3.1 Materials

The material substrate is a NiCr alloy that contains a weight percentage of 28.28% Cr, symbolized by Ni28Cr. This kind of material is an oxidation-resistant chromia-forming alloy and its oxidation behavior has been largely studied [4-6]. The chemical composition (weight percentages) is given in Table 1.

Table 1. Chemical composition (weight percentages) of Ni28Cr alloy

Ni	Cr	Si	Mn	C (ppm)	P (ppm)	S (ppm)
71.2	28.28	< 0.01	< 0.01	230	30	40

In order to find out the influence of reactive elements on the mechanical properties of the chromia layers, we have also performed some groups of experiments using the reactive elements Y_2O_3 or Zr.

For the series with Y_2O_3, the samples were treated by the technique of physical vapor deposition (PVD) [24], and were exposed in a chamber for different exposure time in order to vary the quantity of Y_2O_3 in the alloy. The principle consists in sputtering a target of yttrium oxide with a beam of ions (Ar+) produced by using a radiofrequency source. The atoms of the Y_2O_3 target are then sputtered and deposited on the surface of the substrate with an energy varying from a few electron volts to a hundred electron volts.

The machine used is NORDIKO-3000. During the experiment, the gun releasing a beam of ions (Ar+) was kept at very low pressure, which ranges from 0.1 Pa to 1 Pa. In addition, because the atoms extract off from the target are very energetic, the chamber is maintained at extremely low pressure (0.01 Pa) to avoid their self-collision.
In order to call the sample more easily, we have given code names for the samples Ni28Cr with different exposure times corresponding to different quantities of Y_2O_3 in the alloy, as shown in Table 2:

Table 2. Code name for the sample Ni28Cr with different exposure times

Code name	Reactive element Y_2O_3 exposure time
Y_2O_3_t10	t = 10s
Y_2O_3_t50	t = 50s
Y_2O_3_t100	t = 100s

For the series of Zr, the metallic substrates have been subjected to ionic implantation of zirconium. Three doping fluencies have been applied: $1*10^{15}$, $5*10^{15}$ and $1*10^{16}$ ions.cm^{-2}. The implanter is EATON™NV3206 [24]. The implanter consists of an ion source, an electro-magnet, an accelerator, a beam shaping system and a chamber where the sample is implanted. The Zr^+ ions were obtained by sputtering a source of zirconium with Xe^+ ions that was ionized from the atoms of a neutral gas (xenon). The electro-magnet chamber allowed selecting Zr^+ ions for implantation. After the acceleration system and beam shaping system, the Zr^+ ions are implanted on the sample surface.
The fluence measurement (ions/cm^2) corresponds to the integration of the current measured by an ammeter, for a given surface and during the implantation period. The experiment was performed at room temperature.
In order to call the sample more easily, we also have given code names as shown in Table 3:

Table 3. Code name for the sample Ni28Cr with different doping fluencies

Code name	Reactive elements Zr fluence
Zr1E15	$1*10^{15}$ ions.cm^{-2}
Zr5E15	$5*10^{15}$ ions.cm^{-2}
Zr1E16	$1*10^{16}$ ions.cm^{-2}

3.2 Experimental measurements for stress determination

3.2.1 Experimental setup/conditions

X-ray diffraction (XRD) is extensively applied to determine the elastic strain of crystalline materials As a consequence, it is possible to identify the associated stress by using the method $\sin^2\psi$, as well as the radiocrystalllographic elastic coefficients. However, given that the material is composed of randomly oriented crystallites, Bragg's law is used to determine the changes in distance between the crystallographic planes, considering the diffraction geometry (Fig. 3). Afterwards, rings are generated by using a two-dimensional detector. Based on [25], a relation is provided to turn ψ into a function of θ and γ.

$$\cos\psi = \sin(\theta)\sin(\omega) + \cos(\gamma)\cos(\omega)\cos(\theta), \quad (22)$$

where ψ is the angle between the normal to the surface and the normal to the diffracting planes, 2θ is the angle between the incident beam and the diffracted beam, ω is the incident angle and γ is the angle between the vertical passing through the position of the direct beam and a given position on the diffraction ring (see in Fig. 3).

3.2.2 Data treatment

The untreated data (see an example in Fig. 4) are images of the diffracted rings. It requires further analysis to obtain the stress in the oxide layers. For a material which has no stress, the data should produce perfect circles. An example saved for the NiCr + Cr_2O_3 system is shown in Fig.4.

With the aim of analysing the unprocessed data, the rings have been subdivided into 128 sectors γ with values between {-61.5 ° and + 65.5 °} with a 1° step (Fig. 5).
From these data, it is possible to plot the intensities of each sector γ as a function of 2θ, giving a 1D diffraction diagram. The peaks to be studied for the chromium oxide are (104), (110), (116), which are the most intense and best defined. The 2θ free of stress reference positions are summarized in Table 4.

Table 4. Reference positions for the free of stress diffraction peaks [27]

Plan (hkl) Cr_2O_3	(104)	(110)	(116)
2θ Theoretical (°)	13,25	14,30	21,20

To choose the best simulation for each diffraction diagram, four main distribution functions have been tested to simulate the peaks profile, which are Gauss, Lorentz, Pearson 7 and Pseudo-Voigt. In addition, it is necessary to minimize the influence of the background. The polynomial relationship for the background is tested. The peak distribution and background noise can be simulated either simultaneously or separately.

Fig. 6 shows an example, which simulates the peak forms and the background separately. Given the initial experimental peak, the background is considered as a polynomial relationship. After removing it, the different distribution functions are used to simulate the peak profile.

Fig. 7 shows the results obtained for the different distribution functions. In that case, the simulation results are quite similar for the parameters obtained such as the intensity, the position, and the width of the peak. Finally, to choose the best function, we need to test systematically this procedure by considering a big number of experimental data. All this procedure has been automatized in a Matlab handmade software with the implementation of validity criteria on the fitting quality. By comparing different distribution functions, Pearson 7 distribution function with a background of a polynomial of order 3 is chosen to fit the results.

3.2.3 $\sin^2\psi$ method

When a material is deformed, the distance between crystallographic planes d_{hkl} will extend or contract, which will cause a shift in the rings position in the diffraction pattern. The distance changes between the crystallographic planes can be determined by measuring this angular shift in order to evaluate the elastic deformation.
The reference (x, y, z) is an orthonormal coordinate system linked to the sample. The direction $\vec{e}_{\varphi\psi}$ is the normal to the diffracting plans as shown in Fig. 8. The strain on the direction $\vec{e}_{\varphi\psi}$ is:

$$\varepsilon_{\psi\varphi} = \vec{e}_{\varphi\psi}\bar{\bar{\varepsilon}}\vec{e}_{\varphi\psi} \tag{23}$$

with

$$\vec{e}_{\varphi\psi} = \sin\psi\cos\varphi\vec{e}_x + \sin\psi\sin\varphi\vec{e}_y + \cos\psi\vec{e}_z \tag{24}$$

and $\bar{\bar{\varepsilon}}$ is the elastic strain tensor:

$$\bar{\bar{\varepsilon}} = \begin{pmatrix} \varepsilon_{xx} & \varepsilon_{xy} & \varepsilon_{xz} \\ \varepsilon_{xy} & \varepsilon_{yy} & \varepsilon_{yz} \\ \varepsilon_{xz} & \varepsilon_{yz} & \varepsilon_{zz} \end{pmatrix} \tag{25}$$

The strain along the direction $\vec{e}_{\varphi\psi}$ is:

$$\varepsilon_{\psi\varphi} = \left(\varepsilon_{xx}\cos^2\varphi + \varepsilon_{yy}\sin^2\varphi + \varepsilon_{xy}\sin 2\varphi - \varepsilon_{zz}\right)\sin^2\psi + \left(\varepsilon_{xz}\cos\varphi + \varepsilon_{yz}\sin\varphi\right)\sin(2\psi) + \varepsilon_{zz} \tag{26}$$

The true strain along the direction $\vec{e}_{\varphi\psi}$ can also be obtained by comparing the unstrained distance d_0 between crystallographic planes with the strained distance d.

$$\varepsilon_{\psi\varphi} = \ln\left(\frac{d}{d_0}\right) = \ln\left(\frac{\sin\theta_0}{\sin\theta}\right) \tag{27}$$

By combining Eq. (26) and Eq. (27), it provides a relationship between the angular shift (from θ_0 to θ) and the elastic strain that corresponds to the expected $\sin^2\psi$ strain relationship.

$$\ln\left(\frac{\sin\theta_0}{\sin\theta}\right) = \left(\varepsilon_{xx}\cos^2\varphi + \varepsilon_{yy}\sin^2\varphi + \varepsilon_{xy}\sin 2\varphi - \varepsilon_{zz}\right)\sin^2\psi + \left(\varepsilon_{xz}\cos\varphi + \varepsilon_{yz}\sin\varphi\right)\sin(2\psi) + \varepsilon_{zz} \tag{28}$$

If we assume that elasticity of the material is linear, homogeneous and isotropic, the conversion of elastic strain into stress can be done by using Hooke's model according to:

$$\bar{\bar{\varepsilon}} = \frac{1+\nu}{E}\bar{\bar{\sigma}} - \frac{\nu}{E}\mathrm{trace}(\bar{\bar{\sigma}})\bar{\bar{I}} \tag{29}$$

with trace $\bar{\bar{\sigma}}$ is the first invariant of the stress tensor and $\bar{\bar{I}}$ is the three-dimensional (3D) identity tensor. Under the assumption of transverse isotropy for an in-plane stress state as expected in oxide, we have:

$$\bar{\bar{\sigma}} = \begin{pmatrix} \sigma_{xx} & \sigma_{xy} & 0 \\ \sigma_{xy} & \sigma_{yy} & 0 \\ 0 & 0 & 0 \end{pmatrix} \tag{30}$$

In addition, no shear stress is considered to exist and no stress gradient is assumed.

$$\bar{\bar{\sigma}} = \begin{pmatrix} \sigma & 0 & 0 \\ 0 & \sigma & 0 \\ 0 & 0 & 0 \end{pmatrix} \tag{31}$$

The $\sin^2\psi$ stress relationship is obtained by simplifying Eq. (27)-(31), which indicates the connection between the angular offset, corresponding to the difference between θ_0 and θ, and the stress.

$$\ln\left(\frac{\sin\theta_0}{\sin\theta}\right) = \frac{1+\nu}{E}\sigma\sin^2\psi - \frac{\nu}{E}2\sigma \tag{32}$$

By using the radiocrystallographic elastic coefficients Sij, the $\sin^2\psi$ relation becomes:

$$\ln\left(\frac{1}{\sin\theta}\right) = \frac{1}{2}S_{2(hkl)}\sigma\sin^2\psi + 2S_{1(hkl)}\sigma - \ln(\sin\theta_0) \tag{33}$$

The slope of this line corresponds to $\frac{1}{2}S_{2(hkl)}\sigma$ and the intercept corresponds to $2S_{1(hkl)}\sigma - \ln(\sin\theta_0)$. As the radiocrystallographic elastic coefficients (Table 5) are already available for different families of planes (hkl), the stress in the oxide can then be calculated for these families (104), (110), (116).

Table 5. Radiocrystallographic elastic coefficients for different families of (hkl) planes at 1073K, 1173K and 1273K [28]

1073K

	Cr_2O_3 (104)	Cr_2O_3 (110)	Cr_2O_3 (116)
S_1(TPa)	-0.824	-1.018	-0.805
0.5*S_2 (TPa)	3.987	4.557	3.927

1173K

	Cr_2O_3 (104)	Cr_2O_3 (110)	Cr_2O_3 (116)
S_1(TPa)	-0.821	-1.014	-0.802
0.5*S_2 (TPa)	3.993	4.559	3.934

1273K

	Cr_2O_3 (104)	Cr_2O_3 (110)	Cr_2O_3 (116)
S_1(TPa)	-0.817	-1.010	-0.800
0.5*S_2 (TPa)	3.999	4.561	3.941

In order to fit the $\sin^2\psi$ curves , various criteria of quality have also been defined in the calculation procedure. As an example, one criterion corresponds to the confidence interval around the linear fit, which can control the elimination of abnormal points. Furthermore, the intensity coefficient of the fit and the difference between the first point and the last point of the linear fit are also used to evaluate the quality of the fit. Once all these criteria are achieved, the fitted curves can be considered to be correct which leads to the corresponding slopes and the stress from the point of view of data

processing. Figure 9 shows an illustrative result obtained for $\psi<0$. The trend for $\psi>0$ is quite similar (not shown).

It corresponds to the (116) peak of the chromium oxide. As mentioned before (Eq.33), the stress can be calculated from the slope. However, this stress is only one time point stress. After repeating this treatment for all the experimental pictures, the stress-time curve for oxide peak (116) can be obtained.

By using the same procedure, we can get the stress-time curves for the different (hkl) oxide families in the oxide and for all the systems. Only the results for one peak are further presented for one system.

3.2.4 Stress vs time results

As an example of results, the thermal solicitation for the sample Ni28Cr is shown in Fig. 10:

By using the method described above, the stress-time curves in oxide are obtained. Fig. 11 show the obtained results.

Fig. 11 evidences that the stress in oxide is compressive. When the temperature changes, the jump of the oxide stress between two plateaus is clearly visible.

4. Optimization process

4.1 Principle for optimization

The method for optimizing the parameters is based on the comparison of the time–dependent stresses (obtained in part 3) and the numerical solution (related to the modelling in part 2). By varying the parameters (the growth strain parameter for oxide (D_{ox}) and the creep parameter for oxide (J_{ox})), the numerical solution can be made as similar as possible to the experimental time-dependent stresses. The way to find the best numerical solution compared to the time-dependent stresses is called optimization of parameters and corresponds to a fitting plateau per plateau.

Firstly, a full modelling by taking into account all the experimental points as well as the modelling with thermal strain has been tested and proved to be not satisfying for the present study. As known in [11], the difference of thermal expansion coefficients α between oxide layer and metal substrate is attributed to the stress jump between plateaus. Using such a modelling to analyze the results in its entirety is more difficult and gives more uncertainty on the optimized parameters, which are D_{ox} and J_{ox}. Thus, from a physical point of view, we chose to optimize the parameters plateau by plateau, which avoids introducing the influence of the thermal expansion coefficients α and the stress jump between plateaus in the parameter's identification process.

Secondly, because of the protection induced by the chromia layer formed at 1273K, no more growth of the oxide layer occurs at lower temperature plateau. This has been verified through the XRD intensity evolution in the oxide phase (not shown). Therefore, D_{ox} can be chosen equal to zero at 973K, 1073K and 1173K with a good confidence [12]. Additionally, the parabolic kinetics parameter (Ap) is equal to zero, because of no growth of oxide at lower temperature plateau. Thus, the only parameter to be identified is J_{ox} for these plateaus.

Moreover, one condition for a correct fitting is that $J_{ox}(T)$ should have a physical meaning. As seen in Eq. (5), the parameter $J_{ox}(T)$ should be described as:

$$J_{ox} = \frac{Cste}{k_B T} \exp\left(-\frac{Q}{RT}\right) \tag{34}$$

where Cste is a constant, k_B is the Boltzmann constant and Q is the activation energy associated to the considered creep mechanism. This equation can be transformed into:

$$\mathrm{Ln}(J_{ox}k_BT) = \mathrm{Ln}(\mathrm{Cste}) - \frac{Q}{R} \times \frac{1}{T} \tag{35}$$

If we draw the curve of $\mathrm{Ln}(J_{ox}k_BT)$ versus $\frac{1}{T}$ for different temperatures, we should get a straight line and the activation energy Q can be deduced from the slope of this line. By drawing the curve $\mathrm{Ln}(J_{ox}k_BT)$ versus 1/T using J_{ox} for temperature plateaus at 973K, 1073K and 1173K, the theoretical value of J_{ox} for 1273K can be extrapolated. By using this theoretical value of J_{ox} for 1273K at first iteration, we can fit the first temperature plateau at 1273K and optimize the values of both J_{ox} and D_{ox} at the same time.

4.2 Optimization of J_{ox} for the lower temperature plateaus with $D_{ox} = 0$

The simulation results are be obtained for the 973K, 1073K and 1173K temperature plateaus, except for the first temperature plateau at 1273K [29].

Figs. 12.a.b.c show that the simulations are not as good as expected. Maybe it is because the D_{ox} value has been fixed for all these temperature plateaus. If D_{ox} was remained as variable and if the fitting procedure have considered both J_{ox} and D_{ox} at the same time, then the fit quality could be better from a mathematical point of view. However, Rakotovao [24] has showed that the microstructure was constructed only during the first temperature plateau and the thickness and grain size do not change any more for the lower temperature plateau. Thus, it is quite reasonable to assume $D_{ox} = 0$ for these temperature plateaus, even if the simulation quality does not appear as so good for some plateaus. We require mainly physical consistence of the identification process. There may also be other possible physical explanations. For example, the creep parameter of metal (J_m) and the Norton exponent of metal (N_m), which are very sensitive and difficult to identify. It will be considered in our future work for further investigations.
Moreover, we have tested the value of Nox. It is also discussed in previous works [29]. The Norton exponent Nox can be extracted by the asymptotic approach for a long time and often leads to a unit exponent. This behavior is generally interpreted as boundary creep mechanisms [30]. Indeed, the Nabarro-Herring and Coble creep mechanisms lead to a Norton exponent close to 1. The value for Nox can be chosen very confidently [21]. Therefore, for layer oxide, the Nox value is assumed systematically equal to 1 for the considered oxides. In addition, it is possible to check once again that Nox is close to the unit thanks to the optimization error function (not presented here). This was achieved successfully, as presented in Panicaud et al [31].

4.3 Optimization of J_{ox} and D_{ox} for the first plateaus

From Figs. 12.a.b.c, the different creep parameters J_{ox} have been identified for the temperature plateaus at 973K, 1073K and 1173K. Then, by plotting the curve $\mathrm{Ln}(J_{ox}k_BT)$ versus 1/T, a theoretical and numerical value of J_{ox} for 1273K can be extrapolated.

Fig. 13 shows that the creep parameter J_{ox} for temperature plateaus at 973K, 1073K and 1173K have a perfect linear fit. From this linear fit, the J_{ox} value for 1273K can be predicted.

Finally, with this theoretical value of J_{ox} for 1273K, we can fit the first temperature plateau at 1273K and optimize simultaneously the values of J_{ox} and D_{ox}.

Fig. 14 fits the parameter J_{ox} and D_{ox}. Since this is the first plateau, we assume that the stress is 0MPa at the very beginning of our experiment. This assumption can be well verified by the experience data in many samples.

5. Results and analyses

The previous procedure has been reproduced for all the materials considered in the present study and presented in section 3.1.

5.1 Results for the raw material Ni28Cr alloy

The results concerning J_{ox} ($Pa^{-1}s^{-1}$) and D_{ox} (m^{-1}) obtained from the optimization procedure for the raw material Ni28Cr alloy are presented in Table 6.

Table 6. Results for raw material Ni28Cr alloy

Temperature (K)	1273	1173	1073	973
J_{ox} ($Pa^{-1}s^{-1}$)	$4.68*10^{-15}$	$1.48*10^{-15}$	$6.20*10^{-16}$	$1.45*10^{-16}$
D_{ox} (m^{-1})	2513.5	0	0	0

We can draw the linear fit of $Ln(J_{ox}k_BT)$ versus $\frac{1}{T}$ for Ni28Cr, as shown in Fig.15:

The activation energy Q can be calculated from the slope of this line that is 1.22 keV. Fig. 15 indicates that the creep parameter J_{ox} decreases with a lower temperature, which is consistent with the thermal activation of the creep mechanism

5.2 Results for the yttria-coated materials

5.2.1 Determination of the creep parameter J_{ox} and the activation energies

5.2.1.1 Sample $Y_2O_3_t10$

For the yttria-coated samples, there is no thermal load plateau at 973K. The simulation of experimental data of sample $Y_2O_3_t10$ and optimization procedure for plateau 1073K, 1173K and 1273K are shown in Figs. 16.a.b.c.

Figs. 16.a.b.c show the simulations of J_{ox} for sample $Y_2O_3_t10$ with N_{ox}=1, which is the lowest deposited yttria amount. Fig. 16.c indicates that the evolution of stress is the result of a balance between two phenomena, which are the increase of stress mainly caused by the growth of oxide layer and the relaxation of stress mainly caused by creep behavior. At the beginning of the plateau 1273K, the increase of stress holds a dominant position, until around 714s when the stress reaches -646MPa. After that, the relaxation of stress mainly holds the leading position for mechanical balance.

Fig. 16.a and Fig. 16.b indicate that there is no increase of stress, in relation to the protection of oxide layer formed at 1273K. The latter also indicates that the oxide layer formed at high temperature prevents the formation of oxide layer at lower temperatures. This phenomena has been discussed in previous works [12]. In the present work, a full thermomechanical model is applied that obtains the same conclusion, which also comfirms that the oxide layer thickness does not increase when temperature jumps were applied towards lower values. The stress was released along 2 isothermal periods for 6h (3h for 1173K and 3h for 1073K). The stress release along the temperature plateaus is 280 MPa at 1173 K and 90 MPa at 1073 K.

The results concerning J_{ox} ($Pa^{-1}s^{-1}$) and D_{ox} (m^{-1}) obtained from the optimization procedure for the yttria-coated material $Y_2O_3_t10$ are presented in Table 7.

Table 7. Results for the yttria-coated material $Y_2O_3_t10$

Temperature (K)	1273	1173	1073
J_{ox} ($Pa^{-1}s^{-1}$)	$1.19*10^{-15}$	$1.09*10^{-16}$	$2.96*10^{-17}$
D_{ox} (m^{-1})	4633.1	0	0

As discussed before, D_{ox} equals to zero for plateaus at 1073K and 1173K. In addition, the creep parameter J_{ox} decreases as the temperature decreases.

5.2.1.2 Sample $Y_2O_3_t50$

The simulation of experimental data of sample $Y_2O_3_t50$ and optimization procedure for plateau 1073K, 1173K and 1273K are shown in Figs. 17.a.b.c.

Figs. 17.a.b.c show the simulation of J_{ox} for sample $Y_2O_3_t50$ with Nox=1, which has the same conclusion as Figs. 16.a.b.c. For the plateau at 1273K, the evolution of stress is the result of a balance between two phenomena. Until 1470s when stress reaches -319MPa, the increase of stress holds a dominant position. After that, the relaxation of stress holds the leading position.

Fig. 17.a and Fig. 17.b indicate that there is no increase of stress. The stress was released along 2 isothermal periods for 6h (3h for 1173K and 3h for 1073K). After temperature jumps, stress relaxation is always considered with a decreasing amplitude with the isothermal temperature plateau (150MPa at 1173K and 10MPa at 1073K). Particularly, for the plateau at 1073K, the change of stress is very low, compared to the stress change at 1173K and 1273K, which means that during the isothermal periods at 1073K there is barely the relaxation of stress that is to say the creep behavior is so weak.

The results concerning J_{ox} ($Pa^{-1}s^{-1}$) and D_{ox} (m^{-1}) obtained from the optimization procedure for the yttria-coated material $Y_2O_3_t50$ are presented in Table 8.

Table 8. Results for the yttria-coated material $Y_2O_3_t50$

Temperature (K)	1273	1173	1073
J_{ox} ($Pa^{-1}s^{-1}$)	$7.50*10^{-16}$	$8.62*10^{-17}$	$5.51*10^{-18}$
D_{ox} (m^{-1})	3660.5	0	0

The same results can be extracted as for sample $Y_2O_3_t10$. D_{ox} equals to zero for plateau at 1073K and 1173K. For plateau at 1273K, D_{ox} of $Y_2O_3_t50$ is smaller than D_{ox} of $Y_2O_3_t10$. In addition, the creep parameter J_{ox} decreases as the temperature decreases.

5.2.1.3 Sample $Y_2O_3_t100$

The simulation of experimental data of sample $Y_2O_3_t100$ and optimization procedure for plateau at 1073K, 1173K and 1273K are shown in Figs. 18.a.b.c.

Figs. 18.a.b.c show the simulation of J_{ox} for sample $Y_2O_3_t100$ with Nox=1, which has the same conclusion as Figs. 16.a.b.c. For the plateau 1273K, untill 2454s when stress reaches -448MPa, the increase of stress holds a dominant position. After that, the relaxation of stress holds the leading position. Fig. 18.a and Fig. 18.b indicate that there is no increase of stress. The stress relaxation amplitude is 60MPa at 1173K and 4MPa at 1073K. For the plateau at 1073K, the change of stress is very close to 0, compared to the stress change of 1173K and 1273K, which means the creep amplitude is lower.

The results concerning J_{ox} ($Pa^{-1}s^{-1}$) and D_{ox} (m^{-1}) obtained from the optimization procedure for the yttria-coated material $Y_2O_3_t100$ are presented in Table 9.

Table 9. Results for the yttria-coated material $Y_2O_3_t100$

Temperature (K)	1273	1173	1073
J_{ox} ($Pa^{-1}s^{-1}$)	$8.21*10^{-16}$	$6.85*10^{-17}$	$1.35*10^{-18}$
D_{ox} (m^{-1})	2666.8	0	0

The same results can be extracted as for sample $Y_2O_3_t10$. D_{ox} equals to zero for plateau at 1073K and 1173K. For the plateau at 1273K, D_{ox} for $Y_2O_3_t100$ is smaller than D_{ox} for $Y_2O_3_t50$ and D_{ox} for $Y_2O_3_t10$. The growth strain parameter D_{ox} decreases with the exposure time, thus with the increase of

the quantity of reactive elements. In addition, the creep parameter J_{ox} decreases as the temperature decreases.

5.2.1.4 Analysis of the J_{ox} ($Pa^{-1}s^{-1}$) results for the yttria-coated materials

The values of J_{ox} as a function of temperature are shown in Fig. 19:

Fig. 19 indicates that the creep parameter J_{ox} increases as the temperature increases, whatever the quantity of yttria introduced is, which confirms the thermal activation of this relaxation mode. The aims of introducing reactive elements is to improve the protective properties of the thermally grown chromia layer under high temperature oxidation and to decrease the oxidation kinetics. By increasing the quantity of yttria coated, the creep parameter J_{ox} decreases at plateau 1073K and 1173K, i.e. the viscoplastic strain is smaller with a large quantity of coated yttria at the same temperature, which means that the reactive element Y_2O_3 is effective. However, at 1273K, the J_{ox} value of the yttria-coated 50s sample is slightly lower than the yttria-coated 100s sample, while the J_{ox} value of the yttria-coated 10s is much higher than the other two samples. The J_{ox} value of the yttria-coated 50s and 100s are close at 1273K, relatively to the one for the yttria-coated 10s sample. We can also draw the linear fit of $Ln(J_{ox} * k_B * T)$ versus $\frac{1}{T}$, as shown in Fig. 20:

Fig. 20 indicates that for the raw material and the yttria-coated materials, the creep parameter J_{ox} decreases with a lower temperature as a proof of the thermal activation of the creep mechanism following an Arrhenius model. In addition, this behavior is observed independently of the amount of yttria introduced. For these {Ni28Cr + yttria-coated + Cr_2O_3} systems, when the yttria amount increases, the slope becomes higher which corresponds to an increase of the activation energy. The activation energy for 10s and 50s yttria deposits are 2.25eV and 2.99eV, which are much higher than the activation energy for the raw material 1.42eV. For the maximum yttria amount, the slope is the highest and the activation energy is then close to 3.89eV. The activation energies have been deduced for all the different materials. The results are shown in Fig. 21:

As Fig. 21 shows, the activation energy increases with the exposure time, thus with the increase of the quantity of reactive element. This evolution is roughly linear.

To determine the elementary mechanisms that govern the viscoplastic behavior of the oxide layer as a function of the amount of yttria deposited, the growth mechanism of the thin oxide layer should be considered at the same time [12]. It is known that the growth mechanism of the thin chromia oxide layers becomes anionic when a sufficient quantity of a reactive element is introduced; the formation of the oxide layer is thus controlled by the internal diffusion of oxygen along the diffusion short-circuits, i.e. the grain boundaries [32]. On the other hand, the relaxation of stresses due to diffusion creep in chromia oxide films containing reactive elements is governed by the diffusion of chromium at the grain boundaries. Indeed, it is generally accepted that if the diffusion rate of the ion moving faster controls the oxidation process, then the creep rate is controlled by the movement of the ion moving more slowly [32-38].

Theoretically, a certain elementary mechanism is associated with an activation energy value. In the present case, the activation energy value of about 1eV is attributed to the anionic diffusion of oxygen O^- while the value of about 2eV is attributed to the cationic diffusion of Cr^+ [39]. Fig. 21 indicates that the activation energy for the raw material is between 1eV and 2eV, which is due to the mixing effect of the anionic and cationic diffusion. Fig. 21 also indicates an increase in energy with the exposure time, whose value is higher than 2eV, which means the creep activation energy is mainly determined by the cationic diffusion of Cr^+. As the movement of the slower ion controls the creep rate and as the reactive elements segregate along the grain boundaries, therefore it slows down the external diffusion of Cr.

Consequently, the activation energy is much higher due to an increase of the quantity of reactive elements.

5.2.2 Determination of the growth strain parameter D_{ox} and the associated activation energies
The results concerning the D_{ox} (m^{-1}) parameters for the yttria-coated material are presented in Fig. 22.

Fig. 22 gives the evolution of the D_{ox} parameter as a function of the exposure time; so when the yttria content increases, the values of D_{ox} decreases. As proposed in Eq.9, the activation energy for the growth strain parameter Q_D can be calculated by:

$$Q_D = -\ln\left(\frac{D_{ox0}}{D_{ox}}\right) RT \tag{36}$$

where D_{ox0} is an initial parameter for the present oxide, as proposed in [5], which is equals to $0.122 m^{-1}$.

Thus, the activation energy for growth Q_D versus exposure time has been plotted in Fig. 23:

Fig. 23 shows that the activation energy for growth Q_D decreases as the exposure time increases. As discussed before in section 2.1.4 for the growth strain parameter D_{ox}, the mechanisms are not yet fully established. The $D_{ox}(T)$ parameter depends on microstructural features and may also depend on temperature [5]. It is thus the driving "force" for stress generation in isothermal condition. The D_{ox} parameter may also be related to the ratio of the cationic/anionic flux occurring within the grain boundaries as the oxide layer grows [15]. Hence, we propose that:

$$D_{ox} = D_{ox0}\, exp\left(\frac{Q_D}{RT}\right) = A\left(\frac{J_{anionic}}{J_{cationic}}\right)^B \tag{37}$$

where A is a parameter which represents the relevance between the growth strain parameter D_{ox} and the ratio of the cationic/anionic flux, B stands for the mode of inward and outward oxide layer growth which is between -1 to 1. In our case, we suppose that B is equals to -1, because of the outward oxide layer growth.

Since both flows follow an Arrhenius dependence, this leads to the fact that the current activation energy corresponds to the difference between the values associated with the anionic and cationic activation energy:

$$D_{ox0}\, exp\left(\frac{Q_D}{RT}\right) = A\left(\frac{exp\left(-\frac{Q_{anionic}}{RT}\right)}{exp\left(-\frac{Q_{cationic}}{RT}\right)}\right)^B \tag{38}$$

which gives us:

$$Q_D = RT(ln(A) - ln(D_{ox0})) + B(Q_{cationic} - Q_{anionic}) \tag{39}$$

where Q_D is the activation energy for the growth, $Q_{anionic}$ is the activation energy for anionic diffusion and $Q_{cationic}$ is the activation energy for cationic diffusion.

According to the results presented in 5.2.1.4, the activation energy Q for creep diffusion is higher when the yttria concentration increases, which means that the cationic flows is reduced. The cationic flows is reduced by the presence of yttria and Q is higher, from which it can be deduced that $Q_{cationic}$ is higher. However, these two activation energies are not the same. In addition, Q_D decreases as the exposure time increases. All these results seem to be in good agreement with Eq.39.

5.3 Results for the zirconium-doped materials

5.3.1 Determination of the creep parameter J_{ox} and the activation energies

5.3.1.1 Sample Zr 1E15

For the zirconium-doped samples, there is no thermal load plateau at 973K. The simulation of experimental data of sample Zr 1E15 and optimization procedure for plateau 1073K, 1173K and 1273K are shown in Figs. 24.a.b.c.

Figs. 24.a.b.c show the simulation of J_{ox} for sample Zr 1E15 with Nox=1, which is the smallest deposited zirconium amount. Fig. 24.c indicates that the evolution of stress is the result of a balance between two phenomena, which are the increase of stress mainly caused by the growth of oxide layer and the relaxation of stress mainly caused by creep behavior. At the beginning of the plateau 1273K, the increase of stress holds a dominant position, until 1014s when the stress reaches -588MPa. After that, the relaxation of stress holds the leading position.

Fig. 24.a and Fig. 24.b indicate that there is no increase of stress, due to the protection of oxide layer formed at 1273K, which proves that the oxide layer formed at high temperature prevents the formation of oxide layer at low temperature. This phenomena has been discussed in previous works [12]. In the present work, a full model is applied that leads to the same conclution, which comfirms that the oxide layer did not increase when temperature jumps were applied towards lower values. The stress was released along 2 isothermal periods for 6h (3h for 1173K and 3h for 1073K). The stress release amplitude along the temperature plateaus is 300 MPa at 1173 K and 75 MPa at 1073 K.

The results concerning J_{ox} ($Pa^{-1}s^{-1}$) and D_{ox} (m^{-1}) obtained from the optimization procedure for the zirconium-doped material Zr 1E15 are presented in Table 10.

Table 10. Results for the zirconium-doped material Zr 1E15

Temperature (K)	1273	1173	1073
J_{ox} ($Pa^{-1}s^{-1}$)	$8.33*10^{-16}$	$1.47*10^{-16}$	$4.68*10^{-17}$
D_{ox} (m^{-1})	3528.4	0	0

As we discussed before, D_{ox} equals to zero for plateau 1073K and 1173K. In addition, the creep parameter J_{ox} decreases as the temperature decreases.

5.3.1.2 Sample Zr 5E15

The simulation of experimental data of sample Zr 5E15 and optimization procedure for plateau 1073K, 1173K and 1273K are shown in Figs. 25.a.b.c.

Figs. 25.a.b.c show the simulation of J_{ox} for sample Zr 5E15 with Nox=1, which has the same conclusion as Figs. 24.a.b.c. For the plateau 1273K, the evolution of stress is the result of a balance between two phenomena. Until 2388s when stress reaches -425MPa, the increase of stress holds a dominant position. After that, the relaxation of stress holds the leading position.

Figs. 25.a and 25.b indicate that there is no increase of stress. The stress was released along 2 isothermal periods for 6h (3h for 1173K and 3h for 1073K). After temperature jumps, stress relaxation is always considered with a decreasing amplitude with the isothermal temperature plateau (250MPa at 1173K and 50MPa at 1073K).

The results concerning J_{ox} ($Pa^{-1}s^{-1}$) and D_{ox} (m^{-1}) obtained from the optimization procedure for the zirconium-doped material Zr 1E15 are presented in Table 11.

Table 11. Results for the zirconium-doped material Zr 5E15

Temperature (K)	1273	1173	1073
J_{ox} ($Pa^{-1}s^{-1}$)	$5.99*10^{-16}$	$1.24*10^{-16}$	$2.41*10^{-17}$
D_{ox} (m^{-1})	2156.7	0	0

The same results can be extracted as for sample Zr 1E15. D_{ox} equals to 0 for plateau 1073K and 1173K. For plateau 1273K, D_{ox} of Zr 5E15 is smaller than D_{ox} of Zr 1E15. In addition, the creep parameter J_{ox} decreases as the temperature decreases.

5.3.1.3 Sample Zr 1E16

The simulation of experimental data of sample Zr 1E16 and optimization procedure for plateau 1073K, 1173K and 1273K are shown in Figs. 26.a.b.c.

Figs. 26.a.b.c show the simulation of J_{ox} for sample Zr 1E16 with Nox=1, which has the same conclusion as Figs. 24.a.b.c. For the plateau 1273K, untill 3438s (3846s for the simulation results) when stress reaches -260MPa, the increase of stress holds a dominant position. After that, the relaxation of stress holds the leading position. Fig. 26.a and Fig. 26.b indicate that there is no increase of stress. The stress relaxation is 164MPa at 1173K and 30MPa at 1073K.

The results concerning J_{ox} ($Pa^{-1}s^{-1}$) and D_{ox} (m^{-1}) obtained from the optimization procedure for the zirconium-doped material Zr 1E16 are presented in Table 12.

Table 12. Results for the zirconium-doped material Zr 1E16

Temperature (K)	1273	1173	1073
J_{ox} ($Pa^{-1}s^{-1}$)	$5.37*10^{-16}$	$8.82*10^{-17}$	$5.35*10^{-18}$
D_{ox} (m^{-1})	1249.1	0	0

The same results can be extracted as sample Zr 1E15. D_{ox} equals to 0 for plateau 1073K and 1173K. For plateau 1273K, D_{ox} of Zr 1E16 is smaller than D_{ox} of Zr 5E15 and D_{ox} of Zr 1E15. The growth strain parameter D_{ox} decreases with the exposure time, which means with the increasing quantity of reactive elements. In addition, the creep parameter J_{ox} decreases as the temperature decreases.

5.3.1.4 The results J_{ox} ($Pa^{-1}s^{-1}$) for the zirconium-doped material

The results concerning J_{ox} ($Pa^{-1}s^{-1}$) of zirconium-doped material are presented in Fig. 27.

Fig. 27 shows the same trend as Fig. 20 for the creep parameter J_{ox}, which decreases when the temperature decreases. The creep parameter J_{ox} decreases as the temperature decreases, whatever is the quantity of zirconium introduced, which confirms the thermal activation of this relaxation mode. For all temperature, the values of J_{ox} decreases with the increasing of the quantity of zirconium introduced, which means the reactive element zirconium is effective.

Since it has been shown that the creep parameters depend on the temperature, it is possible to calculate the activation energies associated to the viscoplastic deformation phenomena in the oxide layer. Such activation energies were determined for each quantity of zirconium added by applying Eq. 35. The activation energy Q is calculated and plotted in Fig. 28.

The activation energy increases with a higher fluence and it has a good linear fit of activation energy versus fluence, which means the surface treatment (doping reactive element Zr) is effective and delays the oxidation rate. For (Ni28Cr + Zr/Cr_2O_3) systems, the activation energies are very close for the raw material and the $1*10^{15}$ ions.cm^{-2} zirconium fluence. It corresponds respectively to an activation energy of 1.42eV and 1.78eV. On the contrary, for the greater zirconium quantity of $5*10^{15}$ ions.cm^{-2} zirconium-doped and $1*10^{16}$ ions.cm^{-2} zirconium-doped, the activation energy is clearly higher as the values are respectively 1.99eV and 2.82eV.

As previously discussed for the reactive element Y_2O_3, to determine the elementary mechanisms that should govern the viscoplastic behavior of the oxide layer as a function of the amount of yttria deposited, the growth mechanism of thin oxide layer should be considered at the same time [12]. It leads to the same conclusions for the reactive element zirconium as for yttria. In particular, the creep rate changes and the activation energy is much higher after this surface modification.

5.3.2 Determination of the growth strain parameter D_{ox} and the associated activation energies

The results concerning D_{ox} for zirconium-doped materials are presented in Fig. 29.

Fig. 29 indicates a decrease for D_{ox} versus fluence for the zirconium-doped material. As Eq.9 proposed, the activation energy for growth Q_D can be calculated. The activation energy for growth Q_D versus exposure time is plotted in Fig. 30.

Fig. 30 leads to the same conclusion as for Fig. 23: the activation energy for growth Q_D decreases as the fluence of zirconium increases. However, as discussed before in section 2.1.4, the growth strain parameter D_{ox} evolution is more complicated because the mechanisms are not yet fully established. The $D_{ox}(T)$ parameter depends on microstructural features and may also depend on temperature [5]. Q_D corresponds to an activation energy for growth. Indeed, the D_{ox} parameter is also determined by the ratio of the cationic/anionic flux occurring within the grain boundaries as the oxide layer grows [15]. Since both flows follow an Arrhenius dependence, this leads to the fact that the current activation energy corresponds to the difference between the values associated with the anionic and cationic flows.

6. Conclusions

The present work is based on the time–dependent stresses evolution that are obtained by treating the results of in-situ high temperature synchrotron diffraction measurements obtained at European Synchrotron Radiation Facility. To identify the unknown or unsure parameters, it has been required to investigate a numerical solution of a full thermomechanical modelling. Therefore, an adapted method has been applied to process the experimental results. By comparing the time–dependent stresses and the numerical solution in least-squares sense, the creep parameter for oxide (J_{ox}) and the growth stress parameter for oxide (D_{ox}) have been optimized. Such parameters have been investigated to determine the activation energy associated to the mechanisms.

Firstly, residual stresses have been determined in oxide phase in a {Cr_2O_3+Ni28Cr} system. Thanks to synchrotron X-ray diffraction, it allows in situ measurements during high temperature thermal loads. We found the best simulations of peak profiles by use of Pearson 7 distribution simultaneously with background fitting. For each sample, over 13,000 pictures were processed by applying then $\sin^2\psi$ method to obtain the time-dependent stresses and 7 samples were treated.

For all the samples, including the yttria-coated samples and zirconium-doped samples, the evolution of stress is the result of mechanical balance between two phenomena, which are the increase of stress mainly caused by the growth of oxide layer and the relaxation of stress mainly caused by viscoplastic behavior related to creep mechanisms. At the beginning of the plateau at 1273K, the increase of stress by growth strain holds a dominant position. After the minimun stress, the relaxation of stress mainly holds the leading position for mechanical balance. For the plateau at 1173K and 1073K, there is no increase of stress except during the temperature change between 2 plateaus, in relation to the protection of oxide layer formed at 1273K. The stress is released along this 2 isothermal periods for 6h. The latter also indicates that the oxide layer formed at high temperature prevents the formation of oxide layer at lower temperatures.

Secondly, the thermomechanical modelling of this oxide/metal systems has been successfully implemented. Using Matlab software and a classic Runge-Kutta method, the creep parameter for oxide (J_{ox}) and the growth stress parameter for oxide (D_{ox}) have been identified for all the considered samples.

The aims of introducing reactive elements is to improve the protective properties of the thermally grown chromia layer under high temperature oxidation. By increasing the quantity of yttria coated or zirconium doped, the viscoplastic strain is proved to be smaller with a large quantity of coated yttria or doped zirconium at the same temperature, which means that the reactive element Y_2O_3 and Zr are effective.

For the raw material, for the yttria-coated materials and for the zirconium-coated materials, the creep parameter J_{ox} decreases with a lower temperature as a proof of the thermal activation of the creep mechanism following an Arrhenius model. In addition, this behavior is observed independently of the amount of yttria or zirconium introduced. For this {Ni28Cr + yttria-coated/zirconium-doped + Cr_2O_3} systems, when the reactive elements amount increases, the slope of the Arrhenius curve becomes higher which corresponds to an increase of the activation energy. The creep activation energy is mainly determined by the cationic diffusion of Cr^+. As the creep rate is controlled by the movement of the ion moving more slowly and as the reactive elements segregate along the grain boundaries, therefore it slows down the external diffusion of Cr. Therefore, the activation energy is much higher due to an increase of the quantity of reactive elements.

Thirdly, by increasing the quantity of yttria coated or zirconium doped, the growth strain parameter D_{ox} decreases. In addition, the activation energy for growth Q_D is calculated, which decreases as the exposure time increases or the doping fluence increases. The D_{ox} parameter may also be related to the ratio of the cationic/anionic flux occurring within the grain boundaries as the oxide layer grows. An interpretation of this effect has been proposed.

With such an approach, we better understand the underlying physical mechanisms, and especially those responsible for the creep behavior. With the presence of reactive elements, the surface properties and creep behavior is modified. The viscoplastic strain is smaller with a large quantity of coated yttria or doped zirconium at the same temperature. In addition, by increasing the quantity of yttria coated or zirconium doped, the growth strain parameter D_{ox} also decreases. Thus, the reactive element Y_2O_3 and Zr are effective and they can increase the lifetime of the metallic alloys.

Data availabality

The raw data required to reproduce these findings are available.

References

[1] M. Schütze, Protective Oxide Scales and Their Breakdown, NJ, 1991.
[2] P. Kofstadt, High Temperature Corrosion, London, 1998.
[3] A.M. Huntz, B. Pieraggi, Oxydation des matériaux métalliques, Hermès Science, Paris, 2003.
[4] B. Panicaud, J.-L. Grosseau-Poussard, Z. Tao, F. Rakotovao, G. Geandier, P.-O. Renault, P. Goudeau, N. Boudet, N. Blanc, Frequency analysis for investigation of the thermomechanical mechanisms in thermal oxides growing on metals, Acta Mechanica. 228 (2017) 3595–3617. https://doi.org/10.1007/s00707-017-1899-z.
[5] B.Panicaud, J.-L. Grosseau-Poussard, M. Kemdehoundja, J.-F. Dinhut, Mechanical features optimization for oxide films growing on alloy, Computational Materials Science. 46 (2009) 42–48. https://doi.org/10.1016/j.commatsci.2009.02.003.

[6] Z.J. Tao, F. Rakotovao, J.L. Grosseau-Poussard, B. Panicaud, Determination of Stress Fields and Identification of Thermomechanical Parameters in a Thermally Grown Oxide under Thermal Cycling Loadings, Using Advanced Models, Advanced Materials Research. 996 (2014) 896–901. https://doi.org/10.4028/www.scientific.net/AMR.996.896.
[7] J.L. Ruan, Y. Pei, D. Fang, Residual stress analysis in the oxide scale/metal substrate system due to oxidation growth strain and creep deformation, Acta Mechanica. 223 (2012) 2597–2607. https://doi.org/10.1007/s00707-012-0739-4.
[8] D.P. Whittle, J. Stringer, Improvements in High Temperature Oxidation Resistance by Additions of Reactive Elements or Oxide Dispersions, Philosophical Transactions of the Royal Society A: Mathematical, Physical and Engineering Sciences. 295 (1980) 309–329. https://doi.org/10.1098/rsta.1980.0124.
[9] J. Stringer, The reactive element effect in high-temperature corrosion, Materials Science and Engineering: A. 120–121 (1989) 129–137. https://doi.org/10.1016/0921-5093(89)90730-2.
[10] S. Chevalier, What did we learn on the reactive element effect in chromia scale since Pfeil 's patent?, Materials and Corrosion. 65 (2014) 109–115. https://doi.org/10.1002/maco.201307310.
[11] J. Lemaitre, J.L. Chaboche, Mécanique des matériaux solides, Dunod, Paris, 2001.
[12] F. Rakotovao, B. Panicaud, J.L. Grosseau-Poussard, Z. Tao, G. Geandier, P.O. Renault, P. Girault, P. Goudeau, N. Blanc, N. Boudet, G. Bonnet, In situ Synchrotron X-Ray diffraction study of high-temperature stress relaxation in chromia scales containing the reactive element yttrium, Acta Materialia. 159 (2018) 276–285. https://doi.org/10.1016/j.actamat.2018.07.055.
[13] D.J. Baxter, K. Natesan, Mechanical considerations in the degradation of structural materials in aggressive environments at high temperatures Rev. High Temp. Mater., 5 (1983), pp. 149-250
[14] J.P. Poirier, Creep of Crystals: High-temperature Deformation Processes Metals, Ceramics and Minerals Cambridge University Press, New York, 1985.
[15] D.R. Clarke, The lateral growth strain accompanying the formation of a thermally grown oxide, Acta Materialia. 51 (2003) 1393–1407. https://doi.org/10.1016/S1359-6454(02)00532-3.
[16] B. Panicaud, J.L. Grosseau-Poussard, J.F. Dinhut, General approach on the growth strain versus viscoplastic relaxation during oxidation of metals, Computational Materials Science. 42 (2008) 286–294. https://doi.org/10.1016/j.commatsci.2007.07.017.
[17] Z. Wang, J.-L. Grosseau-Poussard, B. Panicaud, G. Geandier, P.-O. Renault, P. Goudeau, N. Boudet, N. Blanc, F. Rakotovao, Z. Tao, Determination of Residual Stresses in an Oxidized Metallic Alloy under Thermal Loadings, Metals. 8 (2018) 913. https://doi.org/10.3390/met8110913.
[18] B. Panicaud, Contraintes « de croissance » et cinétiques d'oxydation dans des couches d'oxydes thermiques de Fer et de Nickel ; Etude in-situ par Diffraction des Rayons X et modélisation, PhD Thesis, Université de La Rochelle, La Rochelle, France, 2004.
[19] J. Protas, Diffraction des rayonnements : introduction aux concepts et méthodes, Paris, 1999.
[20] Y. Wang, H. Fang, C.L. Zacherl, Z. Mei, S. Shang, L.-Q. Chen, P.D. Jablonski, Z.-K. Liu, First-principles lattice dynamics, thermodynamics, and elasticity of Cr2O3, Surface Science. 606 (2012) 1422–1425. https://doi.org/10.1016/j.susc.2012.05.006.
[21]J.-L. Grosseau-Poussard, B. Panicaud, S. Ben Afia, Modelling of stresses evolution in growing thermal oxides on metals. A methodology to identify the corresponding mechanical parameters, Computational Materials Science. 71 (2013) 47–55. https://doi.org/10.1016/j.commatsci.2013.01.013.
[22] P. L. DeVries , J.E. Hasbun, A First Course in Computational Physics, 2 edition, 2011.
[23] E. Hairer, C. Lubich, M. Roche, The numerical solution of differential-algebraic systems by Runge-Kutta methods, 1989.
[24] F. Rakotovao, Relaxation des contraintes dans les couches de chromine développées sur alliages modèles (NiCr et Fe47Cr): apport de la diffraction in-situ à haute température sur rayonnement

Synchrotron à l'étude du comportement viscoplastique: effets d'éléments réactifs, PhD Thesis, Université de La Rochelle, La Rochelle, France, 2016.
[25] M. François, Unified description for the geometry of X-ray stress analysis: proposal for a consistent approach, Journal of Applied Crystallography. 41 (2008) 44–55. https://doi.org/10.1107/S0021889807051175.
[26] J. Liu, R.E. Saw, Y.-H. Kiang, Calculation of Effective Penetration Depth in X-Ray Diffraction for Pharmaceutical Solids, Journal of Pharmaceutical Sciences. 99 (2010) 3807–3814. https://doi.org/10.1002/jps.22202.
[27] H. Faraoun, H. Aourag, C. Esling, J.L. Seichepine, C. Coddet, Elastic properties of binary NiAl, NiCr and AlCr and ternary Ni2AlCr alloys from molecular dynamic and Abinitio simulation, Computational Materials Science. 33 (2005) 184–191. https://doi.org/10.1016/j.commatsci.2004.12.011.
[28] M.M. Abdullah, F.M. Rajab, S.M. Al-Abbas, Structural and optical characterization of Cr 2 O 3 nanostructures: Evaluation of its dielectric properties, AIP Advances. 4 (2014) 027121. https://doi.org/10.1063/1.4867012.
[29] Z.J. Tao, Experimental study and modelling of mechanical features in an oxide layer under thermal loadings, PhD Thesis, Université de technologie de Troyes, Troyes, France, 2018.
[30] W. R. Cannon, T. G. Langdon, Creep of ceramics, J. Mater. Sci., vol. 18, no. 1, pp. 1–50, 1983.
[31] B. Panicaud, D. Retraint, J.-L. Grosseau-Poussard, L. Li, M. Guérain, P. Goudeau, N. Tamura, M. Kunz, Experimental and numerical study of the effects of a nanocrystallisation treatment on high-temperature oxidation of a zirconium alloy, Corrosion Science. 60 (2012) 224–230. https://doi.org/10.1016/j.corsci.2012.03.033.
[32] H.E. Evans, Stress effects in high temperature oxidation of metals, International Materials Reviews. 40 (1995) 1–40. https://doi.org/10.1179/imr.1995.40.1.1.
[33] T.G. Lanydon, ructural ceramics, California 91360, USA, PROGRESS IN MATERIALS SCIENCE. (n.d.) 255.
[34] K. Przybylski, G.J. Yurek, The Influence of Implanted Yttrium on the Mechanisms of Growth of Chromia Scales, MSF. 43 (1991) 1–74. https://doi.org/10.4028/www.scientific.net/MSF.43.1.
[35] C.M. Cotell, G.J. Yurek, R.J. Hussey, D.F. Mitchell, M.J. Graham, The Influence of Implanted Yttrium on the Mechanism of Growth of Cr203 on Cr, (n.d.) 2.
[36] R.J. Hussey, P. Papaiacovou, J. Shen, D.F. Mitchell, M.J. Graham, The effect of ceria coatings on the high-temperature oxidation of iron-chromium alloys, Materials Science and Engineering: A. 120–121 (1989) 147–151. https://doi.org/10.1016/0921-5093(89)90732-6.
[37] S. Chevalier, G. Bonnet, P. Fielitz, G. Strehl, S. Weber, G. Borchardt, J.C. Colson, J.P. Larpin, Effects of a Reactive Element on isothermal and cyclic oxidation of chromia-forming alloys: SEM/EDX,TEM and SIMS investigations., Materials at High Temperatures. 17 (2000) 247–255. https://doi.org/10.1179/mht.2000.17.2.011.
[38] S. Chevalier, G. Bonnet, G. Borchardt, J.C. Colson, J.P. Larpin, Mechanisms Involved by Reactive Elements upon High Temperature Chromia Scale Growth, MSF. 369–372 (2001) 327–336. https://doi.org/10.4028/www.scientific.net/MSF.369-372.327.
[39] A.F. Carley, P.R. Davies, M.W. Roberts, Activation of oxygen at metal surfaces, Philosophical Transactions of the Royal Society A: Mathematical, Physical and Engineering Sciences. 363 (2005) 829–846. https://doi.org/10.1098/rsta.2004.1544.

Figures captions

Figure 1. Geometry for the oxide growing on a metal

Figure 2. Time step influence on an external growth in the oxide for isothermal conditions

Figure 3. Geometrical configuration of the experiments performed at ESRF. Details on this configuration can be found in [25] and [26]

Figure 4. Diffracted rings for the Ni28Cr + Cr_2O_3 system

Figure 5. Subdivision of the rings of the Ni28Cr + Cr_2O_3 system

Figure 6. Fitting of the peak profiles with or without background

Figure 7. Different peak profiles modelling

Figure 8. Directions and axes of measurement

Figure 9. $\ln\left(\frac{1}{\sin\theta}\right)$ versus $\sin^2\psi$ for the oxide peak (116)

Figure 10. Thermal solicitation for the sample Ni28Cr

Figure 11. Stress evolution in the oxide versus time

Figure 12.a Fitting for parameter J_{ox} at 1173K using different Nox [29]

Figure 12.b Fitting for parameter J_{ox} at 1073K using different Nox [29]

Figure 12.c Fitting for parameter J_{ox} at 973K using different Nox [29]

Figure 13. Linear fit of $\mathrm{Ln}(J_{ox}k_BT)$ versus $\frac{1}{T}$ for extrapolation of J_{ox} at 1273K

Figure 14. Fitting for parameter J_{ox} and D_{ox} at 1273K with Nox = 1

Figure 15. Linear fit of $Ln(J_{ox}k_BT)$ versus $\frac{1}{T}$

Figure 16.a Fitting for parameter J_{ox} at 1073K for Y2O3_t10

Figure 16.b Fitting for parameter J_{ox} at 1173K for Y2O3_t10

Figure 16.c Fitting for parameter J_{ox} and D_{ox} at 1273K for Y2O3_t10

Figure 17.a Fitting for parameter J_{ox} at 1073K for Y2O3_t50

Figure 17.b Fitting for parameter J_{ox} at 1173K for Y2O3_t50

Figure 17.c Fitting for parameter J_{ox} and D_{ox} at 1273K for Y2O3_t50

Figure 18.a Fitting for parameter J_{ox} at 1073K for Y2O3_t100

Figure 18.b Fitting for parameter J_{ox} at 1173K for Y2O3_t100

Figure 18.c Fitting for parameter J_{ox} and D_{ox} at 1273K for Y2O3_t100

Figure 19. J_{ox} versus temperature for the different yttria-coated samples.

Figure 20. Linear fit of $Ln(J_{ox}k_BT)$ versus $\frac{1}{T}$ for yttria-coated materials

Figure 21. Activation energy Q versus exposure time

Figure 22. Growth strain parameter versus exposure time at 1273K

Figure 23. Activation energy Q_D versus exposure time

Figure 24.a Fitting for parameter J_{ox} at 1073K for Zr1E15

Figure 24.b Fitting for parameter J_{ox} at 1173K for Zr1E15

Figure 24.c Fitting for parameter J_{ox} and D_{ox} at 1273K for Zr1E15

Figure 25.a Fitting for parameter J_{ox} at 1073K for Zr5E15

Figure 25.b Fitting for parameter J_{ox} at 1173K for Zr5E15

Figure 25.c Fitting for parameter J_{ox} and D_{ox} at 1273K for Zr5E15

Figure 26.a Fitting for parameter J_{ox} at 1073K for Zr1E16

Figure 26.b Fitting for parameter J_{ox} at 1173K for Zr1E16

Figure 26.c Fitting for parameter J_{ox} and D_{ox} at 1273K for Zr1E16

Figure 27. Linear fit of $Ln(J_{ox}k_BT)$ versus $\frac{1}{T}$ for zirconium-doped materials

Figure 28. Activation energy Q versus fluence of zirconium

Figure 29. Growth strain parameter versus fluence of zirconium at 1273K

Figure 30. The activation energy for growth Q_D versus fluence of zirconium

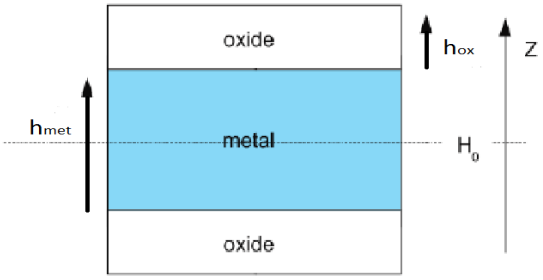

Figure 1.

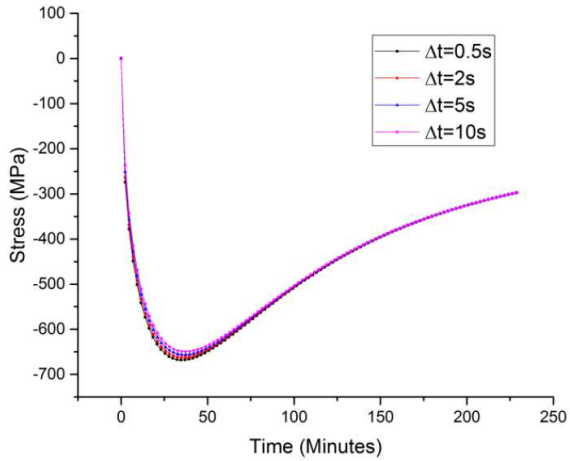

Figure 2.

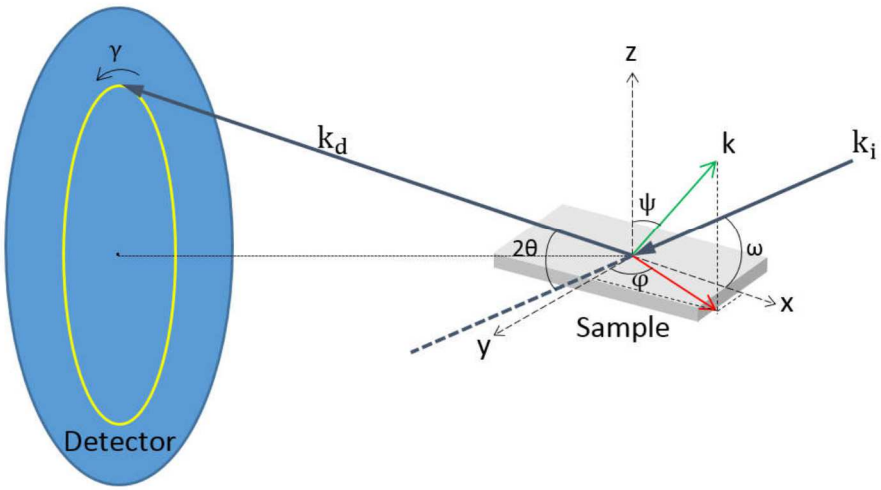

Figure 3.

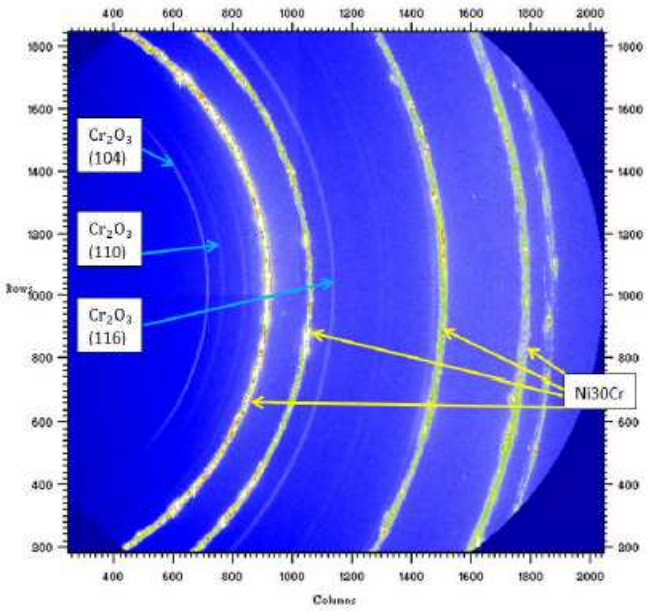

Figure 4.

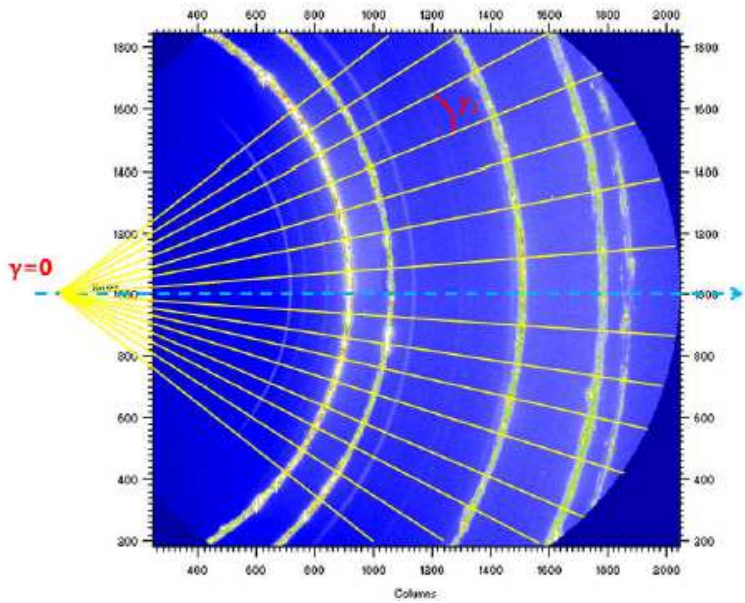

Figure 5.

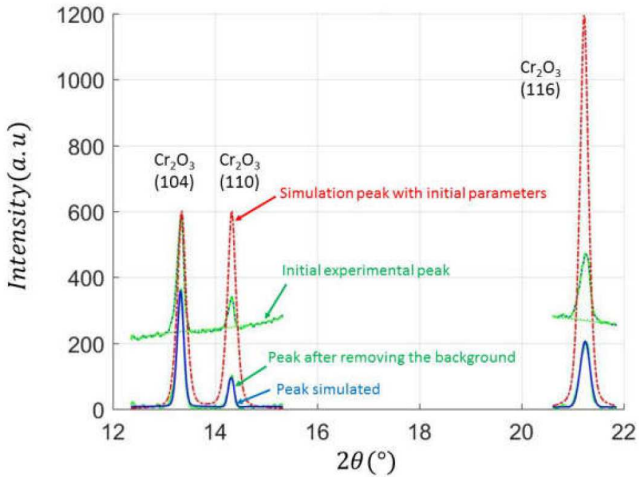

Figure 6.

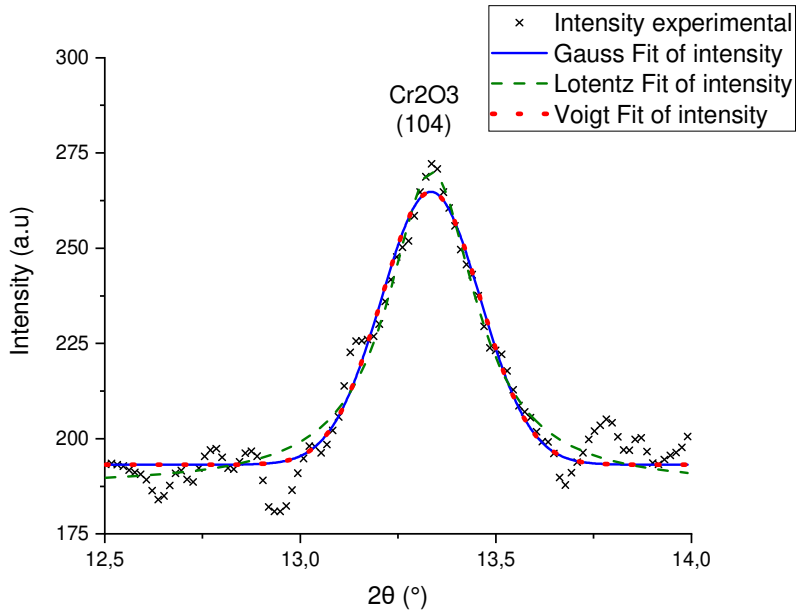

Figure 7.

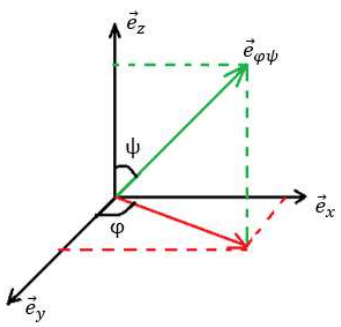

Figure 8.

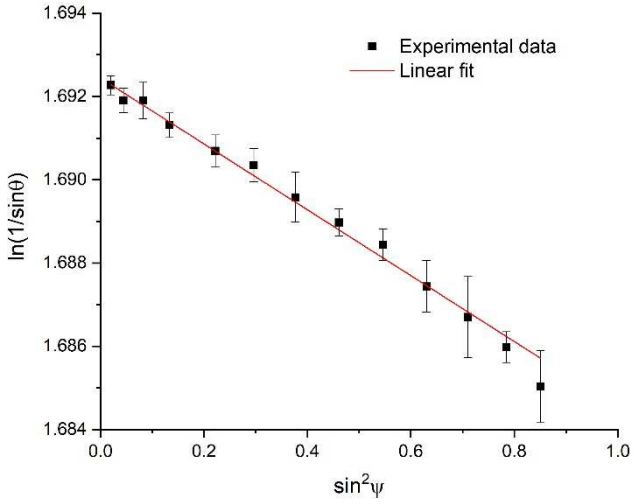

Figure 9.

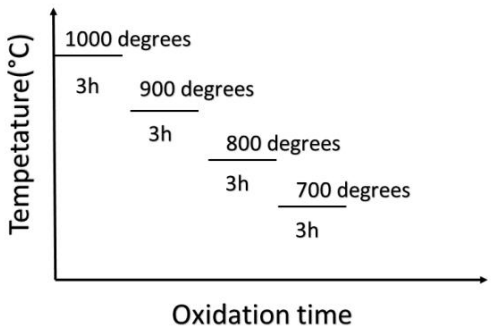

Figure 10.

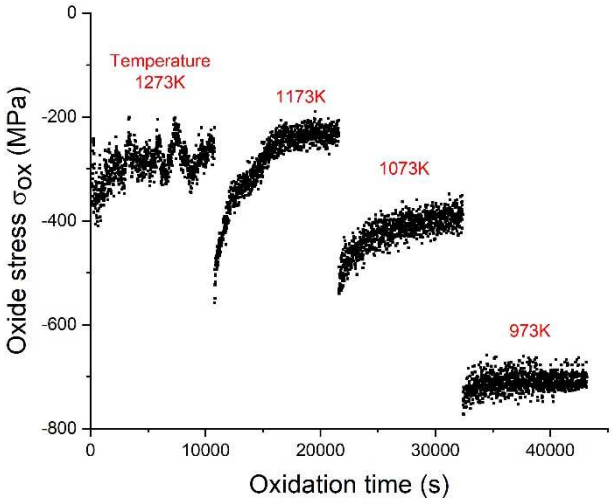

Figure 11.

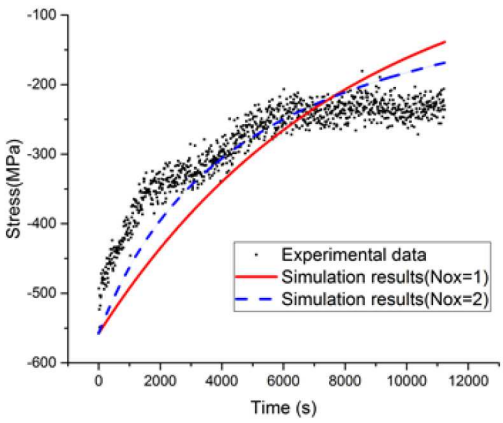

Figure 12.a

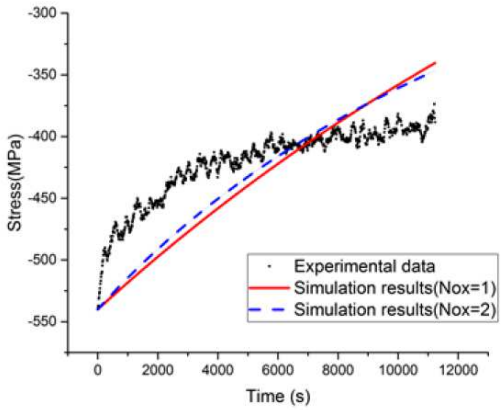

Figure 12.b

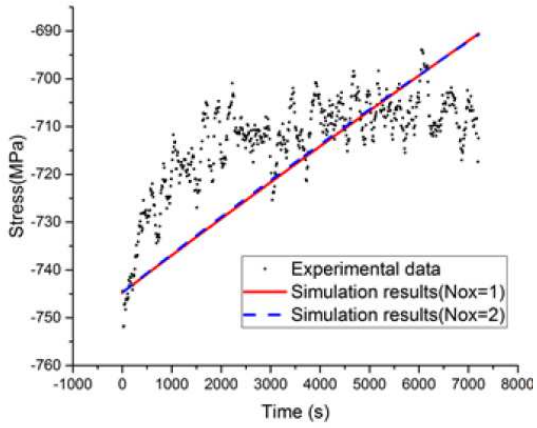

Figure 12.c

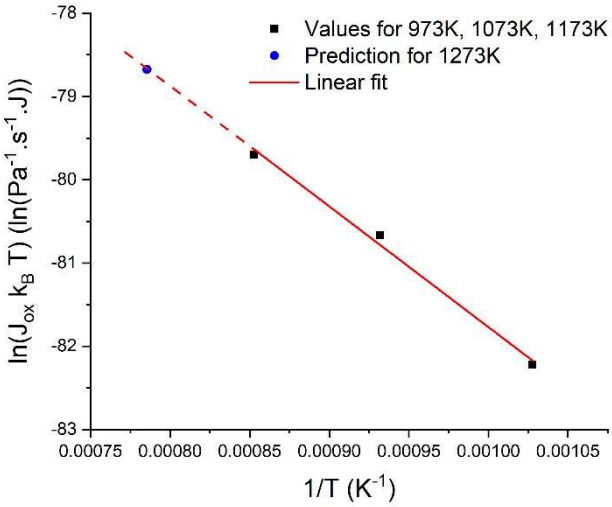

Figure 13.

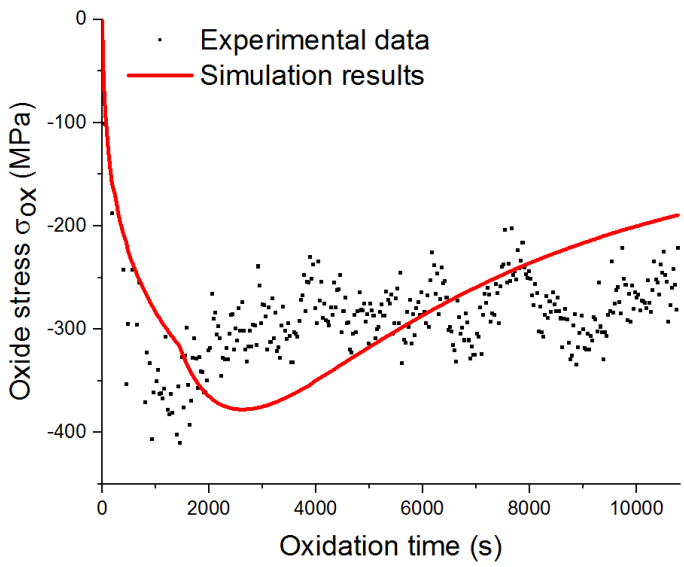

Figure 14.

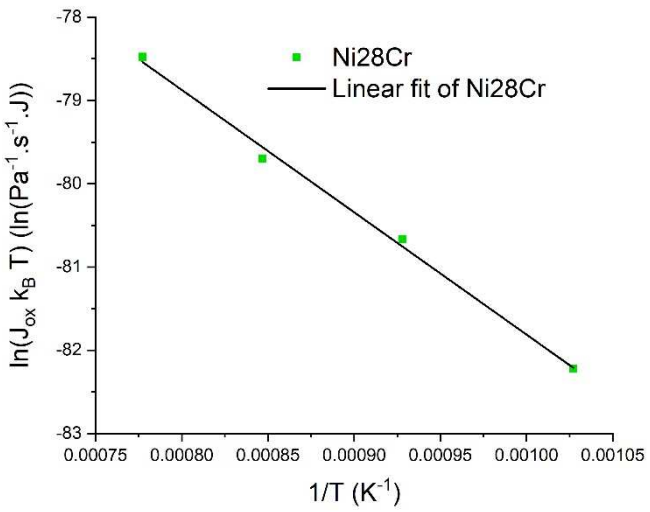

Figure 15.

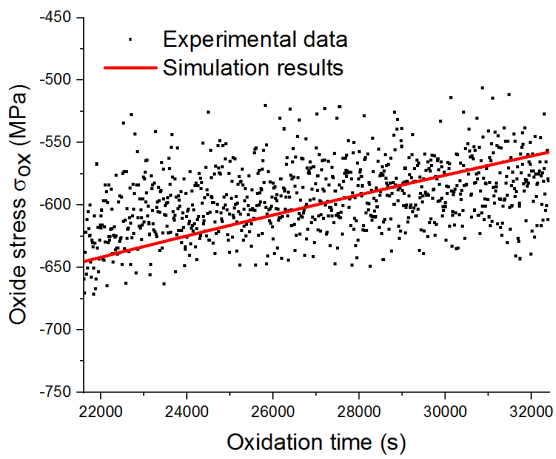

Figure 16.a

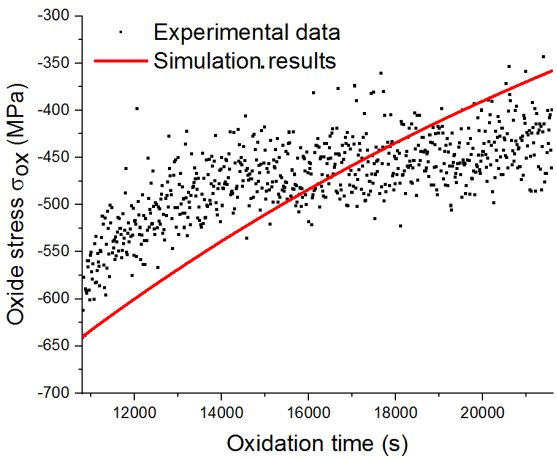

Figure 16.b

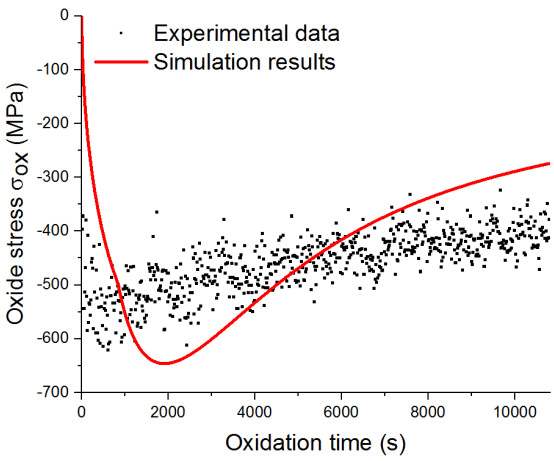

Figure 16.c

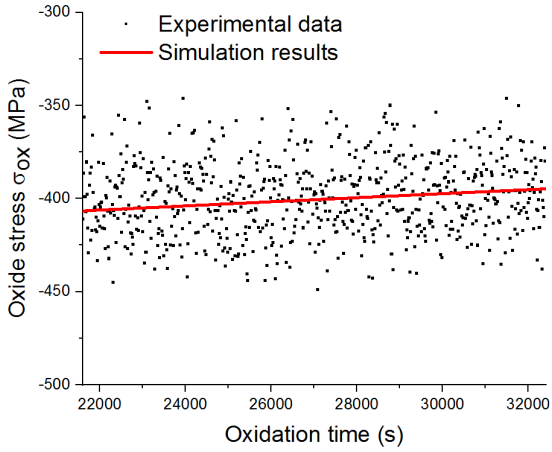

Figure 17.a

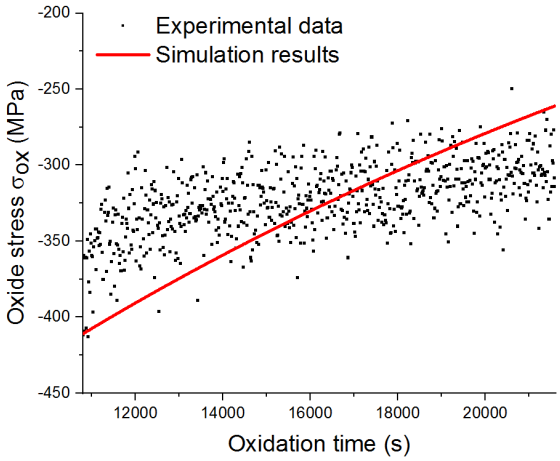

Figure 17.b

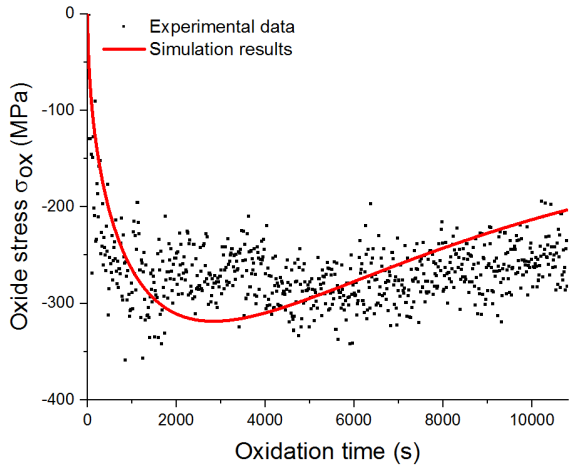

Figure 17.c

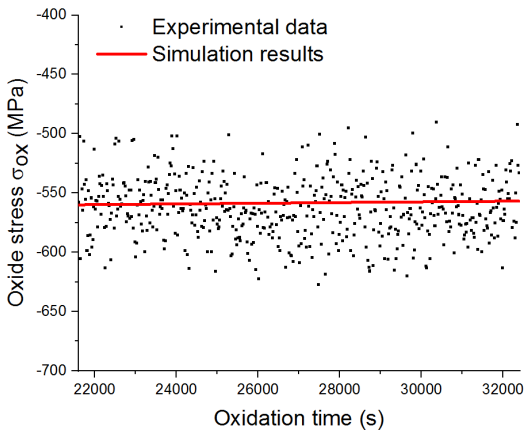

Figure 18.a

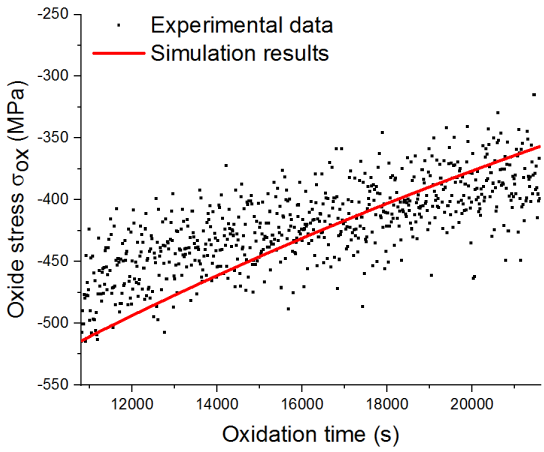

Figure 18.b

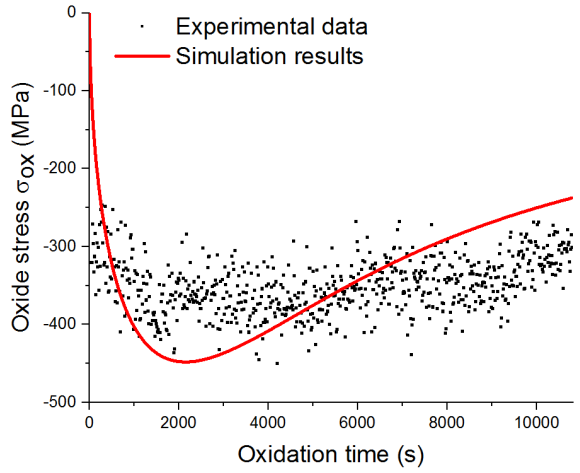

Figure 18.c

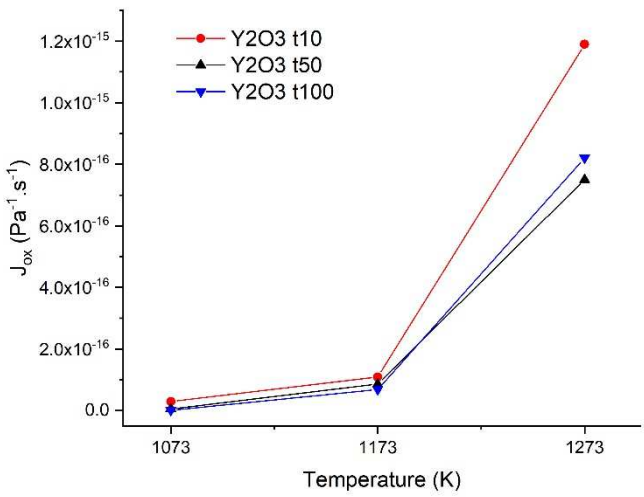

Figure 19.

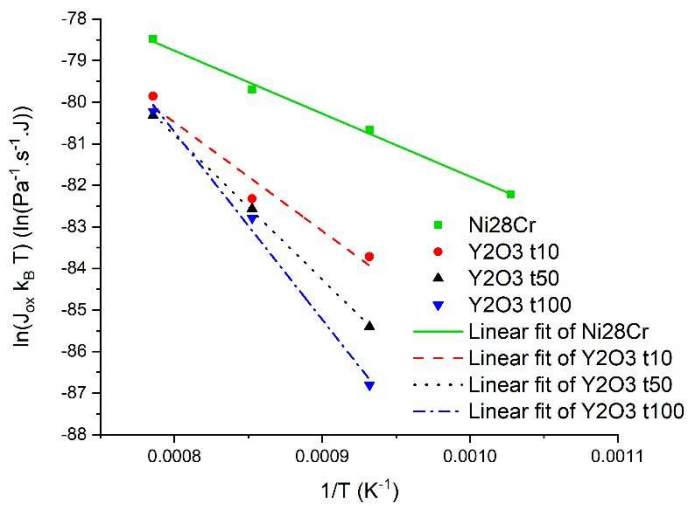

Figure 20.

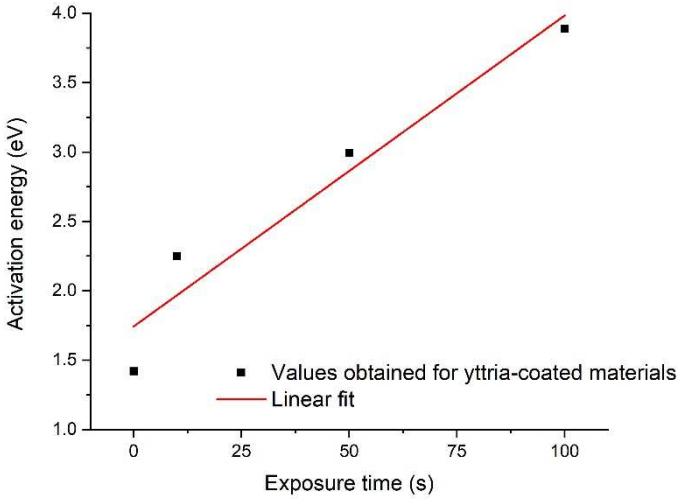

Figure 21.

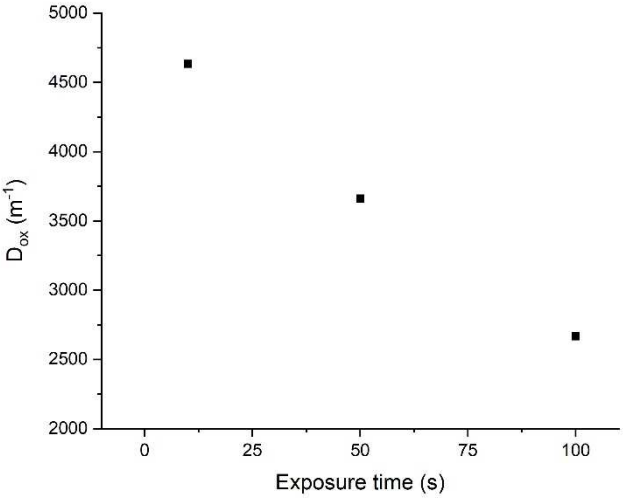

Figure 22.

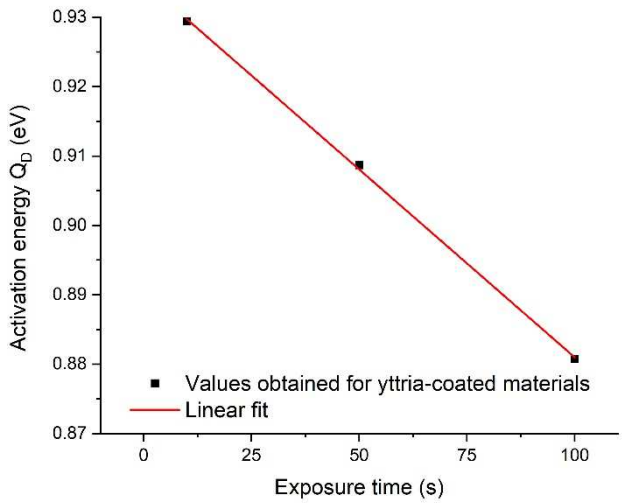

Figure 23.

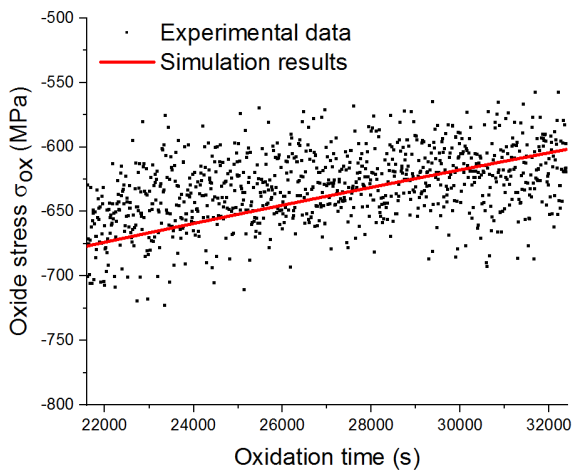

Figure 24.a

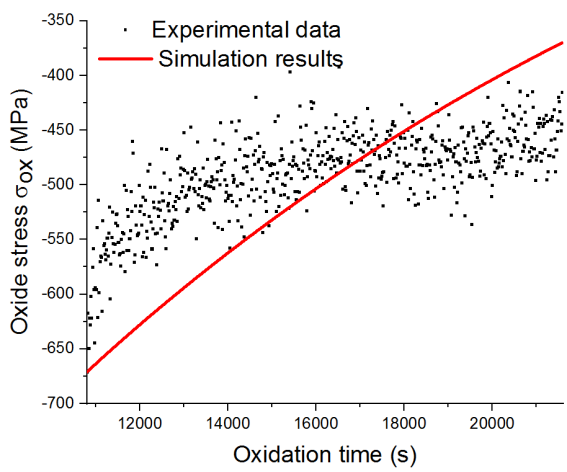

Figure 24.b

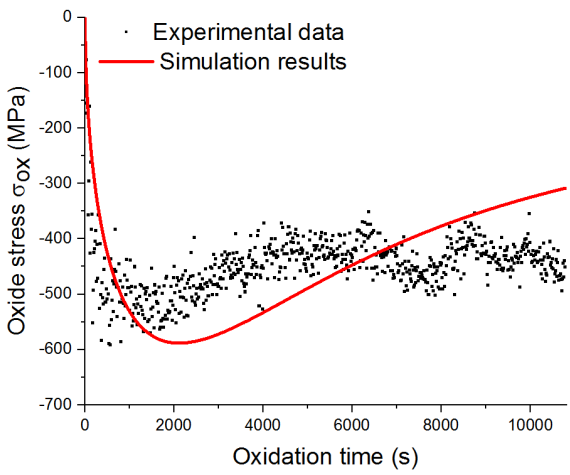

Figure 24.c

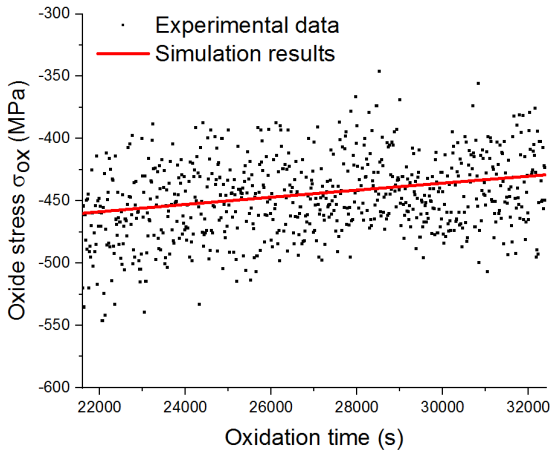

Figure 25.a

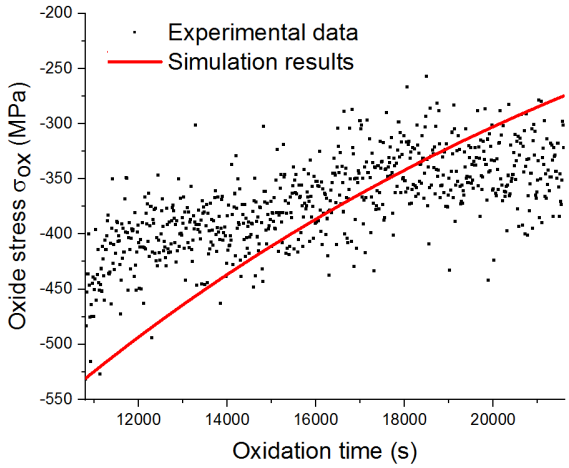

Figure 25.b

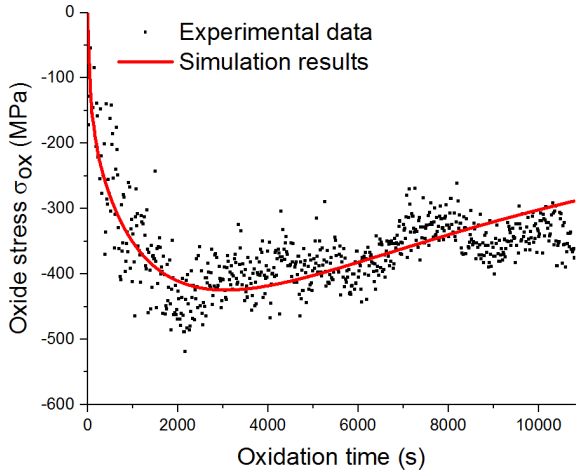

Figure 25.c

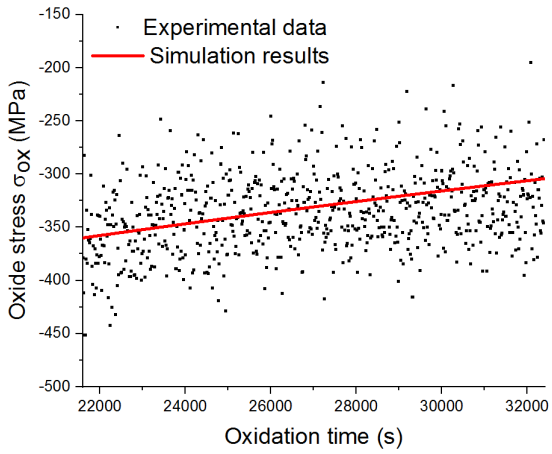

Figure 26.a

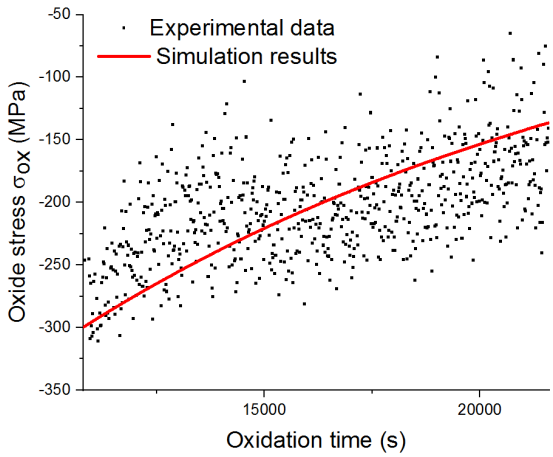

Figure 26.b

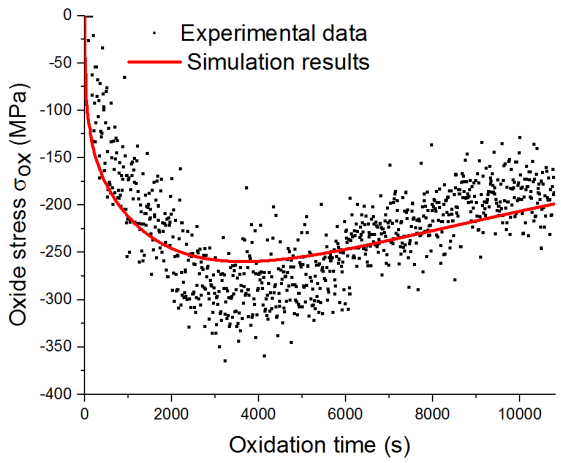

Figure 26.c

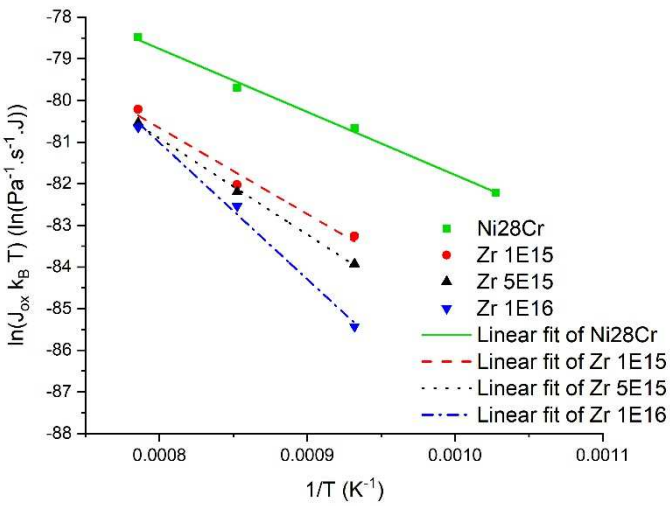

Figure 27.

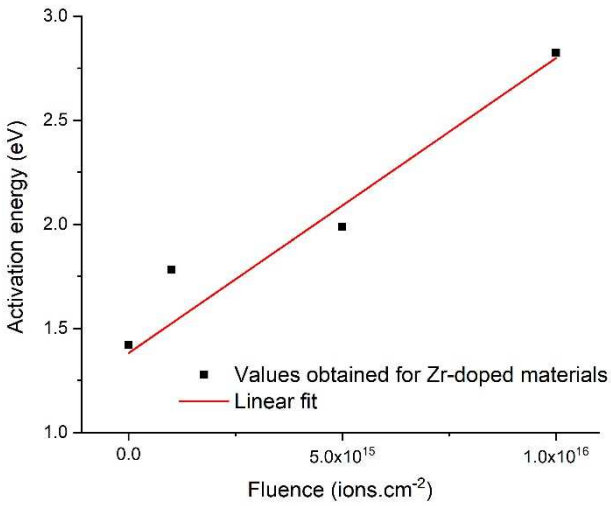

Figure 28.

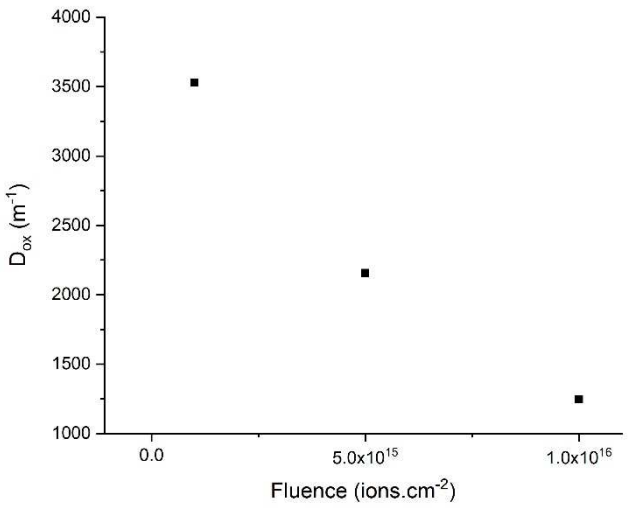

Figure 29.

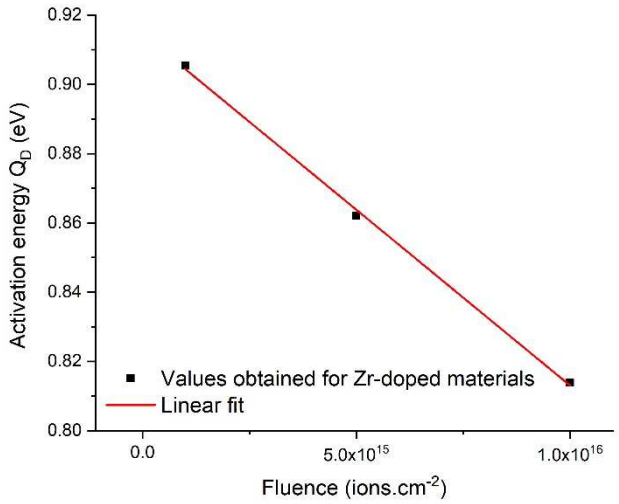

Figure 30.